Title

Dynamic Structural Characterization of Single-Molecule Electronic Devices with Junction Enhanced Raman and Conductance Spectroscopies

Author

Domulevicz, Lucas

Publication Date

2022

Peer reviewed|Thesis/dissertation

Dynamic Structural Characterization of Single-Molecule Electronic Devices with Junction Enhanced Raman and Conductance Spectroscopies

By

LUCAS DOMULEVICZ
DISSERTATION

Submitted in partial satisfaction of the requirements for the degree of

DOCTOR OF PHILOSOPHY

in

Electrical and Computer Engineering

in the

OFFICE OF GRADUATE STUDIES

of the

UNIVERSITY OF CALIFORNIA

DAVIS

Approved:

Joshua Hihath, Chair

Juan Sebastian Gomez-Diaz

Weijian Yang

Committee in Charge

2022

Table of Contents

List of Figures

List of Tables

Glossary

AFM: atomic force microscope

AS: anti-Stokes

BJ: break junction

BPDT: 4-4’-biphenyldithiol

DFT: density functional theory

DI: deionized

EF: enhancement factor

EM: electromagnetic

HOMO: highest occupied molecular orbital

JERCS: junction-enhanced Raman and conductance spectroscopy

LUMO: lowest unoccupied molecular orbital

MEMS: microelectrical-mechanical system

NEGF: nonequilibrium Greens’ function

QI: quantum interference

SEM: scanning electron microscope

SERS: surface enhanced Raman spectroscopy

SNR: signal-to-noise ratio

STM: scanning tunneling microscope

TERS: tip-enhanced Raman spectroscopy

Paper permissions in this dissertation:

Advanced Functional Materials 30.28 (2020): 2000615. – Reproduced with permission of John Wiley & Sons
(https://onlinelibrary.wiley.com/doi/abs/10.1002/adfm.202000615)

ACS Sensors 6.2 (2021): 565-572. – Reproduced with permission of American Chemical Society
(https://pubs.acs.org/doi/10.1021/acssensors.0c02278)

Nature 568 (2019): 78-82. – Reproduced with permission of Springer Nature
(https://www.nature.com/articles/s41586-019-1059-9)

Journal of the American Chemical Society 128.46 (2006): 14748-14749. Reproduced with permission of American Chemical Society
(https://pubs.acs.org/doi/10.1021/ja0648615)

Nano Letters 8.3 (2008): 919-924. Reproduced with permission of American Chemical Society
(https://pubs.acs.org/doi/10.1021/nl073346h)

ABSTRACT

The behavior of charge transport in molecular scale electronics is governed by the innate chemical structure of the molecular system as well as it's coupling to the macroscopic electrical contacts. An in depth understanding of this relationship could allow for the design of nano-electronic devices one atom at a time. Thus far, our understanding of the relationship between molecular structure and transport phenomena has been deduced through systematic studies on families of molecules with subtle variations in their chemical structure which regularly results in conflicting explanations for their underlying behavior. Thus, there is a clear and evident need for a more refined means of directly interrogating the structure of a current carry single molecule.

In this work, we address this need by developing an experimental platform capable of simultaneously measuring the electrical and Raman response of a single molecule junction. This approach allows for mutually verifiable evidence of single molecule sensitivity in our measurements providing a highly reliable platform for investigating the influence of chemical structure on transport properties. By using a scanning tunneling microscope (STM) based break junction system, combined with a commercially purchased confocal Raman microscope, we are able to create single-molecule junctions between the apex of the STM tip and a conductive substrate supporting a monolayer of a target molecule and measure its conductance. Consequently, this nano-junction has a lightning rod effect when illuminated by a Raman excitation source, creating an intense and highly localized field within the junction allowing for detectable Raman scattering originating from a single molecule, thus allowing to probe the structural dynamics of a current-carrying single molecule.

We then demonstrate the utility of this platform in both the field of molecule electronics as well as chemical analysis. We show that through correlations in the conductance signal and Raman scattering from the molecular junction, it is possible to directly observe structural changes in the backbone of a single molecule junction and how this affects its conductance as well as see signatures providing insight on different binding motifs. We then apply this technique to a subset of amino acids and show that, with the aid of machine learning models, it is possible to reliably identify single amino acids using both the conductance and Raman spectral information but not either independently, demonstrating the need and utility for this platform for future advances in single molecule identification.

ACKNOWLEDGEMENTS

First and foremost, I would like to thank Professor Joshua Hihath for acting as my advisor throughout the course my graduate career and for giving me the wonderful opportunity of working in his lab. During my time working Professor Hihath, I have learned much more about what goes into pursuing science and being a decent person than I could have in any textbook. His kindness, patience, and enthusiasm for all forms of science are characteristics I can only hope to emulate as I move forward with my career and life.

I would also like to thank my committee members: Professor Juan-Sebastian Gomez-Diaz and Professor Weijian Yang for their assistance while pursuing my PhD. Their assistance and flexibility is something I greatly appreciate and it has been a pleasure to get to know and work with them as well as their students.

Additionally, I would like to thank all of those who I collaborated with during my research endeavors: Dr. Nayan Kumar Paul and Dr. Firuz Demir for their assistance with theoretical simulations that were essential to understanding the complex systems discussed in this work. I would also like to thank Dr. GW McElfresh for his assistance in developing models for the experimental data in several of the topics of this work.

I would like to extend a special thank you to Dr. Hyunhak Jeong whom I had the pleasure of working with for several years during my graduate career. I have met very few people as intelligent, kind, and hard working as Dr. Jeong and I believe I have become a better person and researcher after being fortunate enough to work with him.

I would like to thank all of my lab mates and students I've had the pleasure of working with during this time: Dr. Mashari Alangari, Dr. Haipeng (Billie) Li, Dr. Cliff McCold, Dr. Taher Ghomian, Dr. Kubra Celik, Dr. Liu Bo, Roohi Ramachandran, Macklin Bolton, Jonathan Marrs,

Zahra Aminiranjbar, and Yichen Gong as well as lab members from Professor Seker's group: Dr. Jovana Veselinovic, Noah Goshi, and Greg Girardi.

I would like to extend a tremendous thank you to my best friend Dr. Christopher Kropiewnicki for continuing to be there for me at a moments notice despite being over 3,000 miles away. Your support means the most to me in good times and bad. Eeyore.

I would like to thank all of my mentors and friends at Wilkes University who inspired me to pursue my graduate degree and have been with me my entire academic career, particularly Dr. Del Lucent, Dr. Amjad Nazzal, Dr. Henry Castejon, and Dr. Gregory Harms. I would not be where I am today without you all believing me and pushing me to pursue my dreams.

I would like to thank my family back home in Pennsylvania for their love and support. My mother and father have sacrificed so much to help me achieve my goals and have been there for me through all my trials and tribulations. Their love and support have not gone unnoticed. Also, I would like to thank my brother and sister for lifting me up when I'm down and helping me push through the hard times. I love you all and will continue to do my best to make you all proud every day.

Finally, I would like to thank, from the bottom of my heart, the family I built here in California with my partner Ashleigh, her mother Brie, her sister Madissen, her Grandmother Sandy, and her Grandfather Don. You all have treated me as a member of your family and supported me in so many ways that I could never repay. Thank you, Ashleigh, for sharing this difficult yet rewarding time in my life. We have already achieved so much, and I can't wait to see what the future holds. Lastly, thank you to our little furry best friends who have brightened my day when I needed it most Mikey, Peabodey, Blueberry, Papaya, Charlotte, and Rosey. I love you all.

In loving memory of Rosey

CHAPTER 1

INTRODUCTION

1.1 The Need for Single-Molecule Conductance and Structural Characterization

Since the concept of using a single molecule as a functional electronic device was first proposed by Aviram and Ratner in 1974[1], tremendous strides have been made in the field leading to theoretical and experimental evidence of single-molecule diodes[2], transistors[3], and photoswitches[4]. Furthermore, devices exploiting the quantum phenomenon unique to these systems have been demonstrated such rectifiers and thermoelectric devices using quantum interference effects[5] and novel spintronic devices[6].

While impressive results have been presented in this field, our intuition and understanding of the interrelationship between chemical structure and the transport properties of single-molecule devices is still underdeveloped. A fundamental understanding of these intricacies is crucial for the development of viable electronics and can lead to the development of nanoscale electronic systems by chemical design.

To this end, remarkable success has been achieved in single-molecule chemistry, in particular, field enhanced Raman spectroscopy for characterizing chemical structure[7] and single-molecule break junction technology for studying electron transport[8], [9]. However, data acquisition in an individual domain is often challenging. Systems utilizing tip-enhanced Raman spectroscopy (TERS) combined with traditional break junction approaches for electron transport[10]–[12] have been demonstrated but often require extreme environmental conditions such as ultra-high vacuum and liquid helium temperatures to operate making them inaccessible. Additionally, the acquisition rates of these methods are long enough that they effectively average

out the dynamics of interest of the system and limit the amount of data necessary for a robust statistical analysis. This barrier has inhibited progress in this area and thus there is a clear and evident need for the further exploration.

1.2 Objective and Innovation

In this dissertation, we aim to develop a technique capable to measuring the conductance and Raman spectral response of a chemical system with single-molecule sensitivity in order to investigate the impact of molecular configuration in single-molecule junctions on their transport properties. By combining a commercially purchased confocal Raman microscope with a custom built, laterally configured, scanning-tunneling microscope (STM) break junction (BJ) system for measuring electrical conductance we were able to demonstrate an experimental platform capable of independently and simultaneously measuring the conductance and Raman scattering of a single-molecule. With this functional platform, we were then able to investigate how changes in the backbone structure of 4-4'-biphenyldithiol molecular junctions influenced their conductive properties as well as develop physical models along the junction's trajectory under the influence of a mechanical strain. We then investigated the influence of anchoring groups on conductance and binding configurations in cysteine based single molecule junctions. Assisted by a machine learning based model, we were able to extract features that mapped Raman spectra to specific conductance distributions and model their physical configurations in the junction using theoretical calculations. As a final demonstration, we show the utility of this technology outside the field of single-molecule electronics by measuring the Raman and conductance response of a subset of amino acids. Using this data, we trained a machine learning model to classify each amino acid. Analysis of the feature importance for classification showed the relative importance of

conductance and Raman features varied between amino acids, highlighting the need for both conductance and Raman spectral data when classifying each molecule.

The major innovation of this work is the multidimensional nature of the characterization demonstrated in the results with superior temporal resolution. The development of this platform and subsequent experimental results show that it is possible to not only reliably measure the Raman and conductive response of a single molecule but also thoroughly investigate its structural dynamics in response to electrical, mechanical, or optical perturbations. The studies presented in this work demonstrate the remarkable success of this platform for not only investigating key questions in the field of molecular electronics but also show that it has far reaching impacts in chemical analysis that may be applied to a variety of fields such as chemistry, biology, engineering, and physics.

CHAPTER 2

Charge Transport in Metal-Molecule-Metal Junctions

2.1 Introduction

In this chapter we will provide a cursory overview of the field of charge transport in the field of single-molecule electronics. The first section of this chapter will provide an overview of the theory of charge transport in single-molecule junctions which will be subdivided into two sections: coherent tunneling and incoherent hopping. The following section will be used to discuss the physical structure of single-molecule devices and how certain features can be chemically tuned to influence the molecule's conductivity. Th next section will provide a brief survey of experimental methods for contacting and measuring the conductance of single-molecule systems with an emphasis placed on the so-called break junction (BJ) method including the strengths and weaknesses of each method. Finally, we will present a discussion on how we are able to infer the effects of chemical structure on the transport properties of single molecules as well as how it is necessary to directly interrogate a molecule's structure during current flow.

2.2 Theoretical Treatment of Charge Transport in Single-Molecule Junctions

The structure of molecular junctions consists of a single molecule sandwiched between two macroscopic electrical contacts (Figure. 2-1a). Much like a bulk crystalline material, a phenomenological description of transport in single-molecule junctions is best presented using an energy band diagram (Figure 2-1b). In this schematic, each electrode is represented by a continuum of states with an associated chemical potential or Fermi energy (μ_L and μ_R for the left and right electrode respectively), while the molecule bridging the contacts is treated as a set of discrete

energy states. The interaction of the continuum states from the electrodes with the states of the molecule results in a broadening of the bridge states, effectively inducing a finite lifetime for occupying the states which in turn describes the strength of the interaction between the electrodes and molecular bridge. The energy scale associated with this interaction, or coupling (Γ), is the defining parameter for determining the charge transport mechanism is single-molecule junctions.

When the coupling is strong relative to the thermal energy of the environment and the charging energy required to place charge directly on the bridge, the transit time for current flowing through the junction is smaller than the mean scattering time and results in minimal interaction with the molecule. This allows the transporting charge to maintain its phase information and the process is said to be coherent.

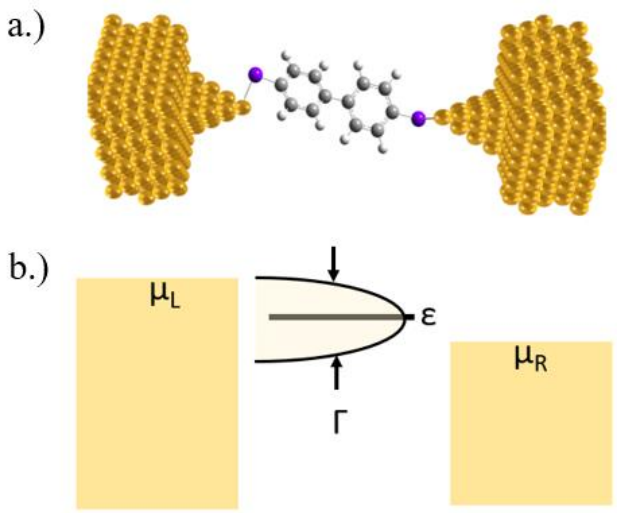

Fig 2-1. (A) Illustration of a molecular junction consisting of two contact electrodes, typically made up of metals such as gold, bridged by a single molecule. (B) Band diagram of a molecular junction depicting the chemical potentials of the electrodes and a discrete energy level of the molecule broadened due to its interaction with the contacts.

In the opposite limit of weak coupling, there is a greater opportunity for charge carriers to exchange energy with the bridge. This exchange results in a dephasing process and the transport mechanism is said to be incoherent.

In the following sections, we will present a brief overview of the most common mechanism in reach limit, namely, coherent tunneling and incoherent hopping. This section will conclude with a discussion of the characteristic features for identifying each mechanism under experimental conditions.

2.2.1 Coherent Transport

When the transit time for an electron to traverse a molecular junction is sufficiently short, such is the case for small molecules covalently bound to the contact electrodes, electrons are expected to transmit coherently, maintaining the phase information contained in the electron's wavefunction. Transport in these systems is typically characterized as electrons tunneling through a potential energy barrier defined by the molecular bridge. In such cases, the conductivity of a molecular wire bridging two macroscopic electrodes is defined by the well-known Landauer formula [13]:

$$G = \frac{2e^2}{\hbar}\sum_{n=1}^{N} T_n \qquad \text{Eq. 2.1}$$

In the above equation, the conductance is represented as a summation of the transmission for the conducting eigenmodes. Thus, in the limit of perfect conduction for a given eigenmode (T=1), a single mode can contribute a maximum of $2e^2/\hbar$ to the total conductance of the system, where e is the charge of the electron and $\hbar$ is the reduced Planck's constant. This prefactor is known as the quantum of conductance, often designated G_0.

In the case of molecular junctions, the transmitting channels are the energy levels associated with the molecule and are no longer discrete due to the broadening from the coupling to the electrodes resulting in the transmission being a function of energy. Given that the transmission is effectively the probability of an electron successfully traversing the junction, one can model the current through the junction as the integral over the conductance multiplied by the probability that a state is occupied [14]:

$$I(V) = \frac{2e}{\hbar} \int_{-\infty}^{\infty} dE\ T(E)[f_L(E) - f_R(E)] \qquad \text{Eq. 2.2}$$

In this equation, $f_{L,R}$ represent the fermi distributions for the left and right electrodes respectively. The difference in fermi distribution represents two competing currents in which charge flow from the left contact to the right and vice versa.

2.2.2 Incoherent Hopping

In contrast to coherent tunneling, when transit time through the molecular junction is significantly high there is greater chance for energy exchanges to occur leading to decoherence effects. The extreme case of this is the completely decoherent process known as hopping transport. This occurs for significantly high transit times that can be associated with longer molecules. In the so-called hopping regime, electrons move sequentially, or "hop", from one part of the molecule to another.

To understand the characteristic properties of the hopping regime, it is helpful to analyze the current using the following toy-model emblematic of this process (Figure 2-2). In this model, the molecular junction is treated as a continuum of states on the left and right sides separated by a set of discrete states for the N sites of the molecular bridge. In this model it also assumed that the

intersite coupling is identical along the bridge and all bridge sites have the same energy which is offset from the Fermi energy of the contacts by ΔE.

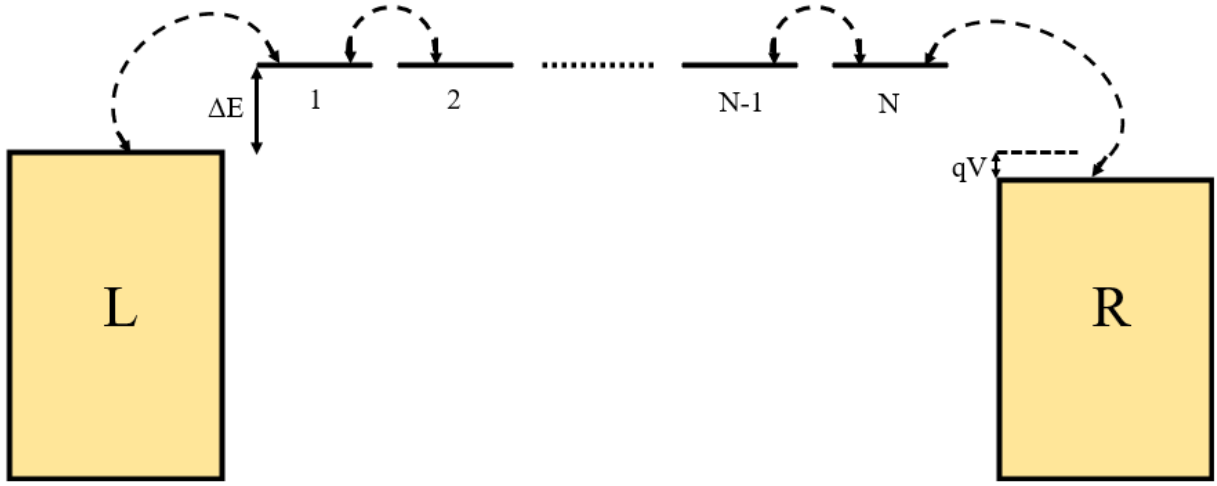

Fig. 2-2. Schematic band diagram of hopping transport in a single molecule junction. The double-sided arrows represent the forward and backward transport between localized energy sites along the molecular bridge.

From here, the current inflow and outflow between two adjacent sites (states j and j+1) using the transfer rates between sites, $k_{i,j}$ (rate of transfer from state j to state i), and the probability of occupation for a given site, P_j, as:

$$I_j = e\left(k_{j+1,j}P_j - k_{j,j+1}P_{j+1}\right) \qquad \text{Eq. 2.3}$$

Since the tunneling between neighboring sites is incoherent, the occupations satisfy a set of classical kinetic rate equations of the form:

$$\dot{P}_j = \frac{dP_j}{dt} = -\left(k_{j-1,j} + k_{j+1,j}\right)P_j + k_{j,j-1}P_{j-1} + k_{j,j+1}P_{j+1} \qquad \text{Eq. 2.4}$$

Under steady state conditions ($\dot{P}_j$=0) it is possible to establish a set of algebraic equations that can be solved for the occupation probabilities. If we make the additional assumption that the internal

rates between sites are equal (i.e. $k_{j,j+1}=k_{j,j-1}=k$), it is possible to establish the following relationships:

$$k_{1,0} = k_L e^{-(\Delta E - eV)/k_B T};\ k_{0,1} = k_L \qquad \text{Eq. 2.5}$$

$$k_{N,N+1} = k_R e^{-\Delta E/k_B T};\ k_{N+1,N} = k_R \qquad \text{Eq. 2.6}$$

In the above equation, ΔE represents the activation of the system understudy and is depicted in figure 2-2.

By substituting the solutions from the set of equations represented by equation 4 and eqs. 5 and 6 into the expression for the current, it is possible to show that the conductance of a molecular system during incoherent hopping transport is given as [13]:

$$G = \frac{e^2}{k_B T} \frac{e^{-\Delta E/k_B T}}{\left[1/k_L + 1/k_R + (N-1)/k\right]} \qquad \text{Eq. 2.7}$$

Of particular importance in this equation is the conductance's dependence on temperature and the number of localized sites. For molecular systems consisting of repeated chemical subunits, the number sites are directly related to the length of the molecule. Neglecting the thermal contribution to the conductance, the conductance decays linearly with increasing molecular length. At appreciable temperatures, set by the activation energy, the conductance depends exponentially on variations in temperature.

2.3 General Structure of Single-Molecule Electronic Devices

Central to the goal of implementing single molecules as functional electronic devices is understanding the underlying transport mechanism responsible for facilitating current flow and how this mechanism is fundamentally related to a molecules chemical structure. Such an intimate

understanding would result in the development of electronics by chemical design, effectively building devices one atom at a time.

While silicon has been the primary material used in the semiconductor industry for decades, carbon is the main element used in single-molecule electronics. This is due to its chemical flexibility which allows it to form a nearly infinite number of compounds with a range of properties and functionalities from mechanically robust diamond to nucleic acids that act as the building blocks for biological life. Given the degree of tunability it can be challenging to discuss the intricacies of molecular devices, however, to simplify this discussion we present a model molecular junction consisting of several units shown below in figure 2-3.

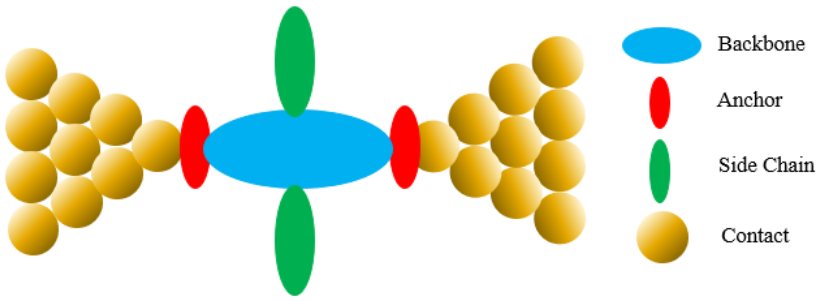

Fig. 2-3. Schematic of a single-molecule junction highlighting four important structural features for tuning the conductance in single-molecule electronic devices. In this schematic, the molecular backbone is highlighted in blue, the terminal anchoring groups are in red, the side chains are shown in green, and the contact electrodes are depicted as gold spheres.

In this model system, the device consists of four distinct regions: macroscopic contacts, anchoring groups, the molecular backbone, and functional side chains. When investigating the transport properties of a single-molecule device, the primary factors that influence its conductivity are the coupling to the electrodes, the alignment of the molecular energy levels with the work function of the contacts, and the localization of the molecular orbitals over the molecule, all of which are influenced by the components of our model system.

Contacting single-molecule systems is one of the primary challenges when testing their transport properties and a variety of materials have been used depending on the situation. Generally, metallic contacts such as copper, silver, or gold are used for their superior conductive properties[15], [16]. Gold is an attractive material due to its limited reactivity allowing for clean surfaces that do not suffer from the effects of oxidation. Despite this attractive prospect, several nontraditional materials such graphene[17] and semiconductors[18] have been used under special circumstances. In the interest of probing magnetic properties such as spin polarized transport, ferromagnetic materials such as cobalt[19] and nickel[20] have also been employed.

The anchor of a single-molecule device acts as the connecting group between the molecular backbone and the contact electrodes. Thus, a choice of material for the contact electrode must be compatible with the anchoring group of the device. While gold is attractive for its limited reactivity, this very same properties reduce the number of viable candidates for anchoring groups, however, there are several candidates for anchoring groups that have an affinity for gold and have been studied extensively for their use in single-molecule junctions[21]–[23]. These anchoring groups include thiols (SH), amines (NH_2), nitriles (CN), and carboxylic acids (COOH). Thiols in particular are used extensively in single-molecule devices due to sulfur's high affinity for gold which provides a mechanically robust contact requiring 1.5 nN of force to rupture[13], [24]. Despite this, it's affinity for gold allows it to bond with the surface in multiple ways depending on the coordination of the gold atoms, resulting in a multitude of distinct conductance distributions for the same molecule[25]. Alternatives, such as amines and nitriles have been shown to create weaker bonds with gold electrodes but produce more reproducible conductance values due to the limited interactions between surfaces atoms[22], [23].

The molecular backbone of a device offers the widest variability in design choice for single-molecule devices. In particular, hydrocarbon-based systems allow for tuning of the degree of conjugation for a given molecule. It has been shown that saturated hydrocarbons such as alkanes[26] are much less conductive than systems with alternating single and double bonds such as alkenes[27] and phenylenes[28] based systems of similar sizes of similar size largely due to the delocalization of their molecular orbitals across the molecule.

While the backbone of the molecule plays an important role for influencing the conductance, functionalizing the molecule with side chains offers a way to fine tune the conductance by either shifting the position of the frontier orbitals relative to the fermi energy of the contact or reducing the degree of conjugation within the molecule. This has been demonstrated in the works of Venkataraman *et al.*[29] where the authors demonstrated the dependence of the conductance on the conformation of the backbone of a set of biphenyl molecules by substituting different side groups to control the torsion angle between the phenyl rings which in turn increased the conjugation along the molecular backbone. The reported result showed that the conductance followed a $\cos^2\theta$ dependence where θ is the angle between the phenyl rings. These results demonstrate the utility of substituents for controlling conductivity as well as suggest the sensitivity of conductance in single-molecule junctions to changes in conformation.

2.4 Single-Molecule Characterization Techniques

Since the emergence of molecular electronics as a field of study, numerous approaches for characterizing the conductance and transport properties of single molecules have been proposed. The central challenge for probing single-molecule junctions is the formation of consistent and reliable atomic contacts with the molecule. To this end, one of the most popular and heavily

utilized approaches is the break junction (BJ) method, or more specifically the scanning tunneling microscope break junction (STM-BJ)[8] and the mechanically controllable break junction (MCBJ)[30]. A depiction of these methods and several others can be seen illustrated in figure 2-4.

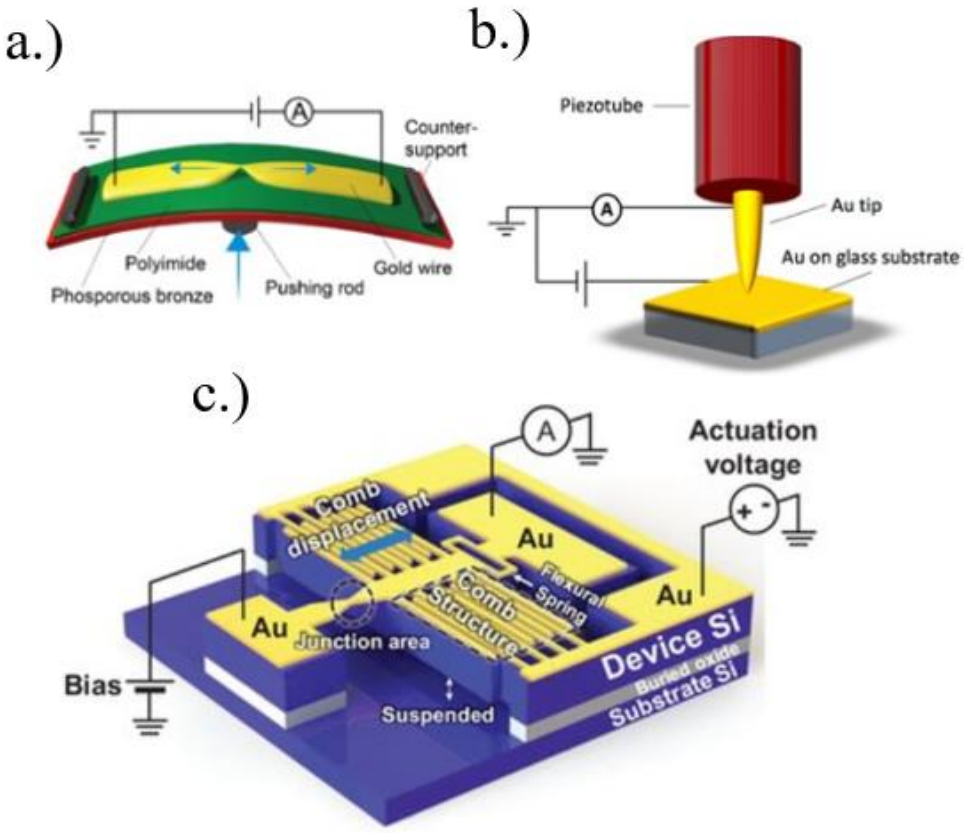

Fig. 2-4. Schematic depictions of break junction architectures used for probing the conductance of single-molecule systems. (a) MCBJ[31], (b) STM-BJ[31], and an on chip micro-electrical-mechanical system (MEMS) based break junction[32].

In STM-BJ systems, atomic contacts with the molecule are formed using the ultra-sharp metallic tips commonly employed in a STM system. The molecules are typically deposited beforehand on a conductive substrate in the form of a self-assembled monolayer (SAM)[33] allowing the STM tip to probe any position on the surface to find a molecule. The advantage of this approach makes it possible to quickly acquire a substantial amount of data that can be used

for a statistical analysis but suffers the drawback of mechanical instability, resulting in a short junction lifetime.

In contrast, the MCBJ approach is far superior in terms of mechanical stability, particularly at low temperatures, enabling the formation of stable junctions that can last on the order of days. The MCBJ method uses a lithographically deposited metallic bow-tie structure on a flexible substrate. The substrate is then deformed at the center by anchoring the ends and using a piezoelectric actuator to bend it. This bending action results in the central region opening and closing in response to the piezoelectric actuator.

Using these BJ configurations, several methods for measuring conductance have been employed. Many of these techniques can be categorized by the control mechanism of the contact electrodes. Two common approaches which will be employed later in this work are the so-called tapping[8] and blinking methods[34]. The tapping method utilizes a closed loop control scheme to rapidly bring the contact electrodes together and apart repeatedly. This method allows the user to measure a significant number of conductance traces in time which can be compiled for a statistical analysis. While the closed-loop control scheme allows for the rapid acquisition of data, the junction lifetime is only on the order of several milliseconds.

Conversely, the blinking method utilizes open-loop control by bringing the contact electrodes to a distance such that set point tunneling current can be measured. Once this target current is measured, the controller is disengaged. This allows for molecules to stochastically form junctions within the gap which appear in the conductance versus time graphs as sudden step-like features or “blinks.” Although much slower for acquiring data, this approach supports longer junction lifetimes.

2.5 Influence of Chemical Structure on Transport Properties

Our understanding of how the structure of a single-molecule junction effects its transport properties is limited to systematic studies on families of molecules with similar structures. For example, it has been demonstrated that with increasing molecular length, conductance decreases exponentially according to[35]:

$$G = G_0 e^{-\beta L} \qquad \text{Eq. 2.8}$$

In equation 2.8, G is the conductance of the molecule, G_0 is the quantum of conductance, β is the characteristic decay length of the molecular family, and L is the length of the molecular device. This result is unsurprising given our previous argument that the mechanism for coherent tunneling can be directly attributed to tunneling phenomena which also decays exponentially with increasing barrier length.

While equation 2.8 presents a convenient closed form relationship between a structural parameter and its conductance, a discussion of the relationship between length and transport properties is much more nuanced. As an example, it has been shown in junctions of 4-4'-biphenyldithiol (BPDT) that mechanical strain on the junction resulting in elongation of the molecule increases its conductance[36]. This behavior results from the reduction of steric hinderance during elongation between the rings which ordinarily are rotated out-of-plane from each other. By lifting this steric hinderance, the rings can planarize, increasing the degree of conjugation over the structure and which increases the overall conductivity.

Our limit in understanding how structural parameters influences transport properties also extends to factors that influence what determines the conduction mechanism. Thus far it has been shown that hopping transport is a temperature dependent process whereas coherent tunneling is not expected to contribute a significant thermal current. As such, characterization of hopping

transport has been historically proved through temperature dependent measurements of the current[37]. However, alternative interpretations of such results have been presented for such phenomena in the coherent tunneling regime. While not stated explicitly the fermi distributions present in equation 2 possess a temperature dependence that can contribute a non-negligible amount to the conductance of a molecule. Li *et al.* [38] have recently demonstrated evidence for temperature dependent tunneling in a family of furan-based oligomers (Figure. 2-5). While this current flow through this family of molecules does show a temperature dependence (Figure. 2-5c), their molecule structure is inherently rigid and lack an internal rotational degree of freedom inhibiting conformation changes that are resultant of overcoming the thermal activation barrier during transport. Instead, by using various models for conductance in both the tunneling and hopping regimes, they were able to attribute this behavior to thermal broadening of the fermi level of the electrodes (Figure. 2-5d). This work demonstrates that characterization of thermally activated incoherent hopping requires more than just information on the temperature dependence on the current and that there is an inherent need for alternative means of definitively characterizing such phenomenon.

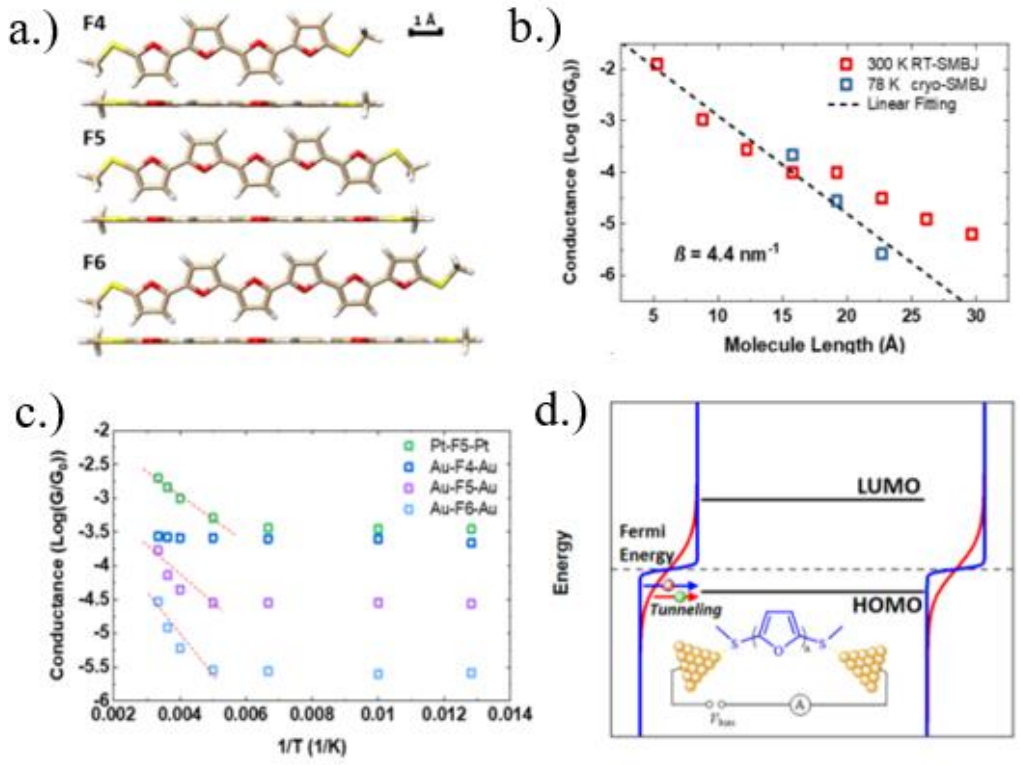

Fig. 2-5. Evidence of temperature dependent tunneling in (a) a family of furan oligomers. (b) Conductance as a function of length for the furan molecules at 300K (red) and 78K (blue). (c) Conductance as a function of temperature for the family of furan molecules. (d) Illustration of the proposed thermally activated tunneling illustrating the broadening of the Fermi energy as the primary mechanism.

While systematic studies of different families of molecules have provided deep insight into the influence of structure on transport, a more direct approach which allows us to both structural and transport properties is inelastic electron tunneling spectroscopy (IETS)[39]. While tunneling is said to be a coherent process, a small portion of the tunneling current may scatter inelastically off the vibrational modes of the molecule which manifest as peaks in the second derivative of the conductance. Information on the normal modes of vibration is directly related to the underlying geometry of the molecule providing us insight into current pathways through it. One issue that IETS faces is the lack of rigorous selection rules offered by other vibrational spectroscopies which provide information on the symmetry of the molecule and vibration and greatly assist in an

analysis. This often makes the interpretation of IETS spectra untenable and limits its applicability for relating structural behavior to transport properties.

CHAPTER 3

Raman Scattering from Plasmonic Nanogaps

3.1 Introduction

Since the initial discovery of the Raman effect by Sir C.V. Raman and K.S. Krishnan in 1928[40], Raman scattering has evolved from a physical oddity to an invaluable experimental technique. With the discovery of SERS and TERS, its popularity has grown exponentially, and it is now regarded as one of the most powerful analytic tools for studying molecular structure.

The goal of this chapter is to present a theoretical and experimental background of Raman scattering as well as shed light on the more recent advances on Raman scattering from single-molecule junctions. Emphasis will be placed on the utility of these methods across multiple disciplines in science and engineering.

To this end, this chapter will introduce the Raman effect by first providing a background in vibrational spectroscopy and then presenting a classical description of Raman scattering, placing an emphasis on how Raman scattered light encodes information on the vibrational structure of the molecular system. Next, we present a survey of the successors to ordinary Raman spectroscopy in the form of field enhanced Raman spectroscopy, namely surface-enhanced Raman spectroscopy (SERS) and tip-enhanced Raman spectroscopy (TERS). The chapter concludes with a discussion of efforts made to combine aspects of TERS with conductance measurements in order to show its utility for applications in molecular electronics as well as single-molecule chemistry.

3.2 The Raman Effect

3.2.1 Vibrational Spectroscopy

To ascertain information about the properties of molecular systems, it is necessary to observe their interaction with measurable systems whose energetics are of a similar scale. Moreover, this energy scale varies between the different degrees of freedom (electronic, vibrational, rotational, etc.). This results in the necessity for various types of spectroscopic techniques used for investigating molecular properties as each region of the electromagnetic (EM) spectrum interacts with a molecule differently. For instance, the energy of electronic transitions in molecules corresponds to wavelengths of light between ~400 to 750 nm placing it in the UV to visible region of the EM spectrum. On the other hand, molecular rotations are much lower in energy and interact readily with microwave excitation sources (~25μm to 1 mm). A diagram illustrating the different regions of the EM spectrum and corresponding energy scales of molecular degrees of freedom can be seen in figure 3-1.

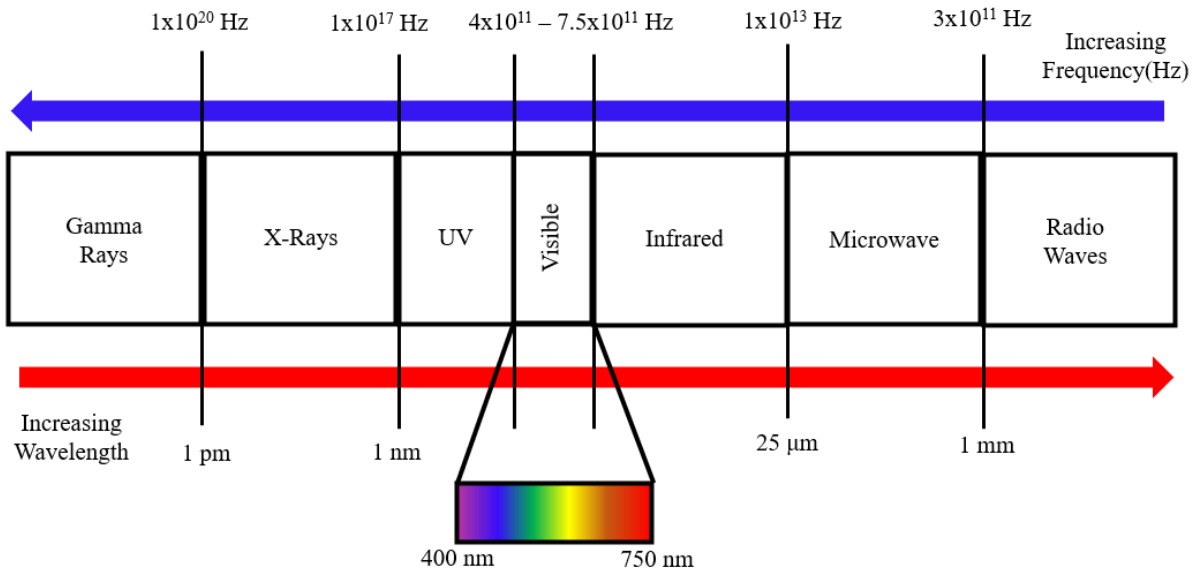

Fig. 3-1. EM spectrum and the corresponding wavelengths and frequencies associated with each region.

The primary focus of this work will be on vibrational degrees of freedom whose transitions occur at longer wavelengths of visible light and continue into the infrared (IR) region. Vibrational spectroscopy is of fundamental importance for identifying chemicals systems and understanding their underlying behavior because it provides substantial information on the geometry, composition, and bond strength of a molecule. To illustrate this, consider the simple case of a diatomic molecule depicted along with its energy profile as a function of bond length in figure 3-2.

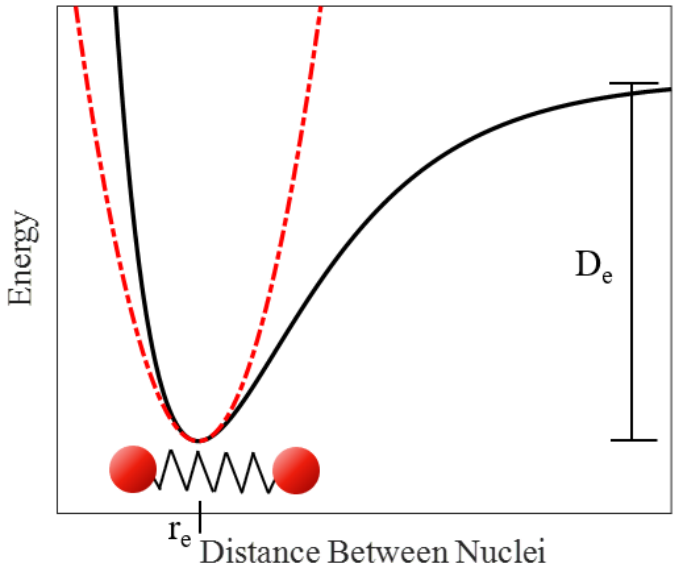

Fig. 3-2. Potential energy profile of a diatomic molecule. The more physical description of a chemical bond is the so-called Morse potential (black) characterized by the well depth (D_e) and the equilibrium bond length (r_e). Under equilibrium conditions, the potential may be approximated as a harmonic potential (red).

In this figure, we see 3 qualitative features: (1) the energy exponentially increases as the bond length is decreased, (2) there exists a minimum energy corresponding to an equilibrium bond length (r_e), and (3) the energy asymptotically approaches a set energy at increasing bond lengths due to dissociation of the constituent atoms. This is the so-called Morse potential and while physically accurate for describing atomic bonds, it is intractable to model an analytic solution for

this potential using quantum mechanics. However, for systems near their equilibrium, this potential can be approximated as a parabola, taking the functional form of,

$$U = \frac{1}{2}kx^2 \qquad \text{Eq. 3.1}$$

This is the well-known harmonic oscillator potential whose behavior is extensively covered in standard undergraduate texts in classical and quantum mechanics[41]. The importance of this approximation is that it allows us to view the bonds of molecular systems simply as systems of springs and masses, with spring constant k and mass m, provided they are near their ground vibrational state. Furthermore, if we can measure the frequency, ω, associated with a chemical bond, we can calculate the corresponding spring constant by,

$$\omega = \sqrt{k/m} \qquad \text{Eq. 3.2}$$

This vibration motion associated with this frequency is known as a vibrational mode.

To extend this analysis to systems of more than 2 atoms, we must consider motion in 3 dimensions. For N atoms, this results in 3N internal degrees of freedom, however, 3 degrees of freedom can be attributed to translational motion and 3 can be attributed to rotational motion resulting in 3N-6 vibrational modes for nonlinear molecules (3N-5 for linear molecules).

3.2.2 Raman Scattering

Next, we must consider how these molecular vibrations interact with light in physically measurable way. When an excitation source illuminates a sample, several interactions can happen, however, two mechanisms that are important for vibrational spectroscopy are absorption and scattering. Absorption is the main mechanism for another type of vibrational spectroscopy called IR spectroscopy in which a photon whose energy matches the energy of vibrational mode is

absorbed by the molecule. Scattering, on the other hand, is responsible for the Raman effect, however, not all scattered photons are due to the Raman effect.

Scattering is a 2-photon optical process in which an incident photon is absorbed by a molecule and instantaneously reemitted. This can happen elastically, in which case the emitted photon is the same energy as the incident photon, or it can happen inelastically resulting in a loss or gain in energy due to the photon's interaction with the molecular vibrations. The process of elastically scattering light is known as Rayleigh scattering and the inelastic process is known as Raman scattering. Furthermore, if the Raman scattered photon experiences a red shift in energy, it is referred to as Stokes scattering, whereas a blue shift is known as anti-Stokes scattering. The magnitude of this shift will be equal to the energy of the interacting vibrational mode. Thus, by measuring this shift it is possible to acquire a chemical fingerprint that is characteristic of a molecule's structure. A Jablonski diagram of the optical processes discussed can be seen in figure 3-3.

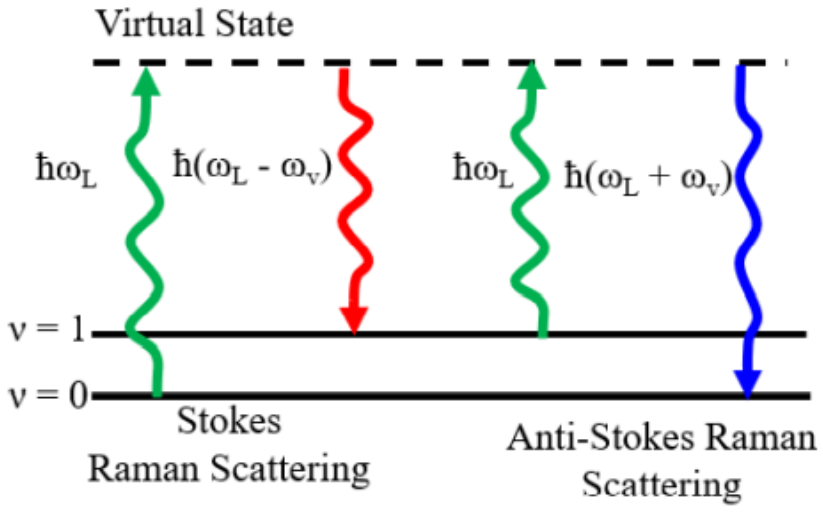

Fig. 3-3. Jablonski diagram depicting both the Stokes and anti-Stokes Raman scattering processes.

A theoretical treatment of the Raman effect is necessary to understand its origin and the physically significant information contained in a Raman spectrum. Since this is an interaction between light and matter, one would expect a full quantum mechanical treatment of both the excitation field and the molecule, however, a semi-classical description of this interaction provides much of the same information without the required rigor and will be the approach taken in this work. For further information on a rigorous theoretical treatment of the Raman effect, the reader is referred to the following reference[42].

Many characteristics of Raman scattering can be deduced using the concepts from elementary electromagnetics. Consider an excitation source producing a time-dependent electric field with frequency ω_L, incident upon a sample,

$$\vec{E}(\omega_L) = \overrightarrow{E_0}\cos(\omega_L t) \qquad \text{Eq. 3.3}$$

At a microscopic level, this induces an alignment of the constituent charges which, to first order, can be described by its dipole moment as,

$$\vec{p} = \alpha\vec{E}(\omega_L) \qquad \text{Eq. 3.4}$$

where $\vec{p}$ is the dipole moment vector and α is the polarizability of the sample. The polarizability is a rank-2 tensor valued quantity describing the linear optical response of the sample due to an excitation source. The amplitude of each tensor element depends on the composition, the strength of the chemical bonds, and underlying geometry of the sample as well as the frequency of the excitation source. At the microscopic scale, the chemical bonds of the system are vibrating, perturbing the charge distribution. To see the effect of this perturbation on the polarizability we can expand it as a Taylor series with respect to the atomic displacement due the kth normal mode, Q_k.

$$\alpha = \alpha_0 + \sum_k \left(\frac{\partial\alpha}{\partial Q_k}\right)_0 Q_k + \frac{1}{2}\sum_{k,l}\left(\frac{\partial^2\alpha}{\partial Q_k \partial Q_l}\right)_0 Q_k Q_l \ldots \qquad \text{Eq. 3.5}$$

This expression can be further simplified by assuming the vibrations of different modes are noninteracting, effectively truncating the series to the first two terms.

$$\alpha = \alpha_0 + \alpha_k Q_k \qquad \text{Eq. 3.6}$$

where α_k is the polarizability change due the vibration of the kth normal mode. In this equation, the displacements take the form of harmonic oscillators for each normal mode,

$$Q_k = Q_k^0 \cos(\omega_k t) \qquad \text{Eq. 3.7}$$

Here, Q_k^0, is the amplitude of the normal mode at the equilibrium position.

By combining equations 3,4,6, and 7, we can see the effect of the vibrations on the induced dipole.

$$\vec{p} = \alpha_0 \vec{E}_0 \cos(\omega_L t) + \alpha_k \vec{E}_0 Q_k^0 \cos(\omega_L t) \cos(\omega_k t) \qquad \text{Eq. 3.8}$$

Using the product of cosines trigonometric identity,

$$\overrightarrow{p} = \alpha_0 \vec{E}_0 \cos(\omega_L t) + \tfrac{1}{2}\alpha_k \vec{E}_0 Q_k^0 \cos\big((\omega_L + \omega_k)t\big) + \tfrac{1}{2}\alpha_k \vec{E}_0 Q_k^0 \cos\big((\omega_L - \omega_k)t\big) \qquad \text{Eq. 3.9}$$

In this equation, we recover much of the phenomenon observed from Raman scattering as well some insight into the underlying physics. From equation 9, it can see that the induced dipole moment is composed of three terms oscillating in time. The first term has a frequency identical to the excitation source whereas the second and third term oscillate at the excitation frequency plus or minus the frequency of the vibrational mode respectively. The first term represents the process of Rayleigh scattering while the second and third terms describe anti-Stokes and Stokes Raman scattering respectively.

Furthermore, the scattering amplitude provides physical insight on the strength of the Raman scattering process for a given vibrational mode. It is unsurprising that the strength of the Raman dipole is directly related to the amplitude of the incident electric field, however, the pre-factors related to the polarizability and normal mode displacement are less obvious. The

polarizability term is often referred to as the selection rules for Raman spectroscopy, namely, a mode is said to be Raman active provided there is a change in the polarizability due to the vibration. This selection rule is well-studied using techniques from group theory to identify whether or not a Raman mode is active given its symmetry. While this topic is beyond the scope of this work, the reader is referred to the following references[43], [44].

Up until this point, the analysis has been entirely classical but has recovered much of the information regarding Raman scattering. To complete this analysis, we must now consider the quantum mechanical nature of the normal mode displacement amplitude. This can be done quite trivially by replacing the classical term in the above equations, $\frac{Q_k^0}{2}$, with the quantum mechanical observable. The following derivation closely follows the derivation presented in the following reference[45]. In this case, the observable will produce two distinct values for Stokes and anti-Stokes due to the transition order. The amplitude is given as,

$$Q_k^{QM} = \begin{cases} \langle n+1|Q_k|n\rangle = (n+1)^{1/2} b_k & (Stokes) \\ \langle n|Q_k|n+1\rangle = n^{1/2} b_k & (anti-Stokes) \end{cases} \quad \text{Eq. 3.10}$$

In this set of equations, $Q_k$is now taken to be the quantum operator for the harmonic oscillator, n designates the respective energy level, and b_k represents the zero-point amplitude given by,

$$b_k = \sqrt{\frac{h}{4\pi\omega_k}} \quad \text{Eq. 3.11}$$

where h is Planck's constant. Since quantum vibrations are bosons, they can be counted using Bose-Einstein statistics. By taking the expectation value of the of the normal mode displacement, we recover the following,

$$\left|Q_k^{QM}\right|^2 = \begin{cases} b_k^2\left(1 + n_k^B(T)\right) & (Stokes) \\ b_k^2 n_k^B(T) & (anti-Stoke) \end{cases} \quad \text{Eq. 3.12}$$

where n_k^B is the known as the Bose factor for the kth vibrational mode given by,

$$n_k^B(T) = \left[exp\left(\frac{h\omega_k}{2\pi k_B T}\right) - 1\right]^{-1} \quad \text{Eq. 3.13}$$

This result provides useful information regarding the amplitude of Raman scattering for both Stokes and anti-Stokes processes. First it is worth noting that both amplitudes rely on temperature or, more generally speaking, phonon population in the ground and excited states. The consequences of this can be seen by substituting equation 12 into equation 9 for the classical analogue and taking the ratio of the anti-Stokes amplitude with the Stokes amplitude. This results in,

$$\frac{A_{anti-Stokes}}{A_{Stokes}} = \frac{n_k^B(T)}{\left(1+n_k^B(T)\right)} = e^{-\frac{h\omega_k}{2\pi k_B T}} \quad \text{Eq. 3.14}$$

Thus, by measuring the intensity of the both the Stokes and anti-Stokes scattering of a vibrational mode, it is possible to gain information on the temperature of the sample. However, this concept may be generalized to account for other interactions as well, as long as there is an exchange of energy between the molecular vibrations of the sample and the interacting phenomena. This will be elaborated on further in upcoming sections.

3.3 Field Enhanced Raman Spectroscopy

3.3.1 Surface Enhanced Raman Spectroscopy

The analysis of the previous section shows the wealth of information that can be obtained from Raman spectroscopy. Despite the prospects offered by this technique, Raman scattering is an inherently weak optical process which limits its utility in a lab setting. However, it is also highly sensitive to a molecule's local environment which can modify both the incident electric field and the chemical nature of the molecule itself potentially enhancing the signal of the Raman scattered radiation. This effect is particularly dramatic for molecules at the surface of rough noble metals

and is the foundation for the field of surface enhanced Raman spectroscopy (SERS). The discovery of the SERS effect has not only promoted Raman spectroscopy as a viable tool for chemical analysis but has also led to numerous scientific advances across multiple disciplines and has led to Raman spectroscopy being regarded as one of the most powerful analytic tools in the physical sciences.

Observations of strong Raman scattering were first reported by Fleishmann *et al.* in 1974 from pyridine molecules adsorbed onto Ag electrodes[46]. The impact of this observation gained increasing momentum years later with the seminal works by Nie *et al.* and Kneipp *et al.* who reported Raman scattering cross sections large enough to resolve the spectra of single molecule[47], [48]. These results sparked an influx of works trying to unambiguously verify the single-molecule nature of the measured spectra[49], [50] as well as determine the mechanisms responsible for this impressive enhancement[51].

The massive enhancements observed in SERS experiments are typically attributed to two dominant mechanisms which we will refer to as electromagnetic (EM) enhancement and chemical enhancement. The EM enhancement factor may be further decomposed into the enhancement of the incident radiation due to coupling of the surface plasmons in the metal and the enhancement of the radiated field due to coupling with the surface plasmons. Chemical enhancement factors, on the other hand, result from a change in the polarizability of the molecule or reorganization of its electronic structure upon adsorption on the SERS substrate. In comparison, chemical enhancement factors (~10-100) are dramatically weaker than EM enhancement effects. For this reason, their contribution to the total enhancement is often neglected as it is also challenging to quantify. Further information on chemical enhancement effects may be found in the following reference[52].

In order to investigate the intricacies of EM field enhancement, it is necessary to first discuss plasmons, or rather, the interactions between plasmons and photons. Plasmons may be loosely defined as the oscillations of charge in a metal whereas the coupling of light to a plasmon at the interface of a dielectric and metal is known as a surface plasmon-polariton. Ordinarily, these plasmons may freely propagate across the interface, however, in the case of a rough surface or nanostructured materials whose dimensions are comparable to the wavelength of the excitation, the mode can no longer propagate and is confined by the geometry of the structure resulting in an intense localized electric field within the region. These fields are referred to as local surface plasmon-polaritons and are fundamentally responsible for the spectacular enhancement seen in SERS measurements [45].

In the previous section, we considered the Raman effect occurring as a 2-step process in which a photon is absorbed and simultaneously re-emitted by an oscillating electric-dipole induced by the photon interacting with the molecular vibrations. This dipole was described by equation 3.4 which assumes the environment to be in free space. In the case of SERS, the dipole is not induced by the incident source but rather a local electric field modified by the environment. The radiative power of a dipole is proportional to the square of its absolute power. To quantify the enhancement, we can then define the enhancement factor prior to re-emission as the ratio of the square magnitudes of the local and incident fields, i.e.

$$M_{Loc}(\omega_L) = \frac{\left|\vec{E}_{Loc}(\omega_L)\right|^2}{\left|\vec{E}_{inc}(\omega_L)\right|^2} \qquad \text{Eq. 3.15}$$

The secondary enhancement, which we will refer to as the radiative enhancement, occurs in a similar manner, i.e. the intensity of the electric field is modified by the local environment as well as the radiation pattern, however, this time the radiation under consideration is at the frequency of the Raman shifted light, ω_R. In this case, we once again define the enhancement factor as the

radiated power compared with re-emission in free space, $M_{Rad}(\omega_R)$. Since the origin of the radiative enhancement is the same as the local field enhancement, the approximation, $M_{Rad}(\omega_R) \approx M_{Loc}(\omega_L)$, is often made. The total EM enhancement factor (EMEF) is then merely the product of individual effects,

$$EMEF = M_{Loc}(\omega_L)M_{Rad}(\omega_R) \approx \frac{|\vec{E}_{Loc}(\omega_L)|^2}{|\vec{E}_{inc}(\omega_L)|^2}\frac{|\vec{E}_{Loc}(\omega_L)|^2}{|\vec{E}_{inc}(\omega_L)|^2}$$

$$= \frac{|\vec{E}_{Loc}(\omega_L)|^4}{|\vec{E}_{inc}(\omega_L)|^4} \qquad \text{Eq. 3.16}$$

This result is the well-known E^4 approximation which makes estimations of the enhancement factors easily accessible. Thus, in order to estimate the enhancement factor for a SERS substrate, the only requirement is to solve Maxwell's equations for the electric field with the boundary conditions imposed by the excited nanostructure.

3.3.2 Tip-Enhanced Raman Spectroscopy

In addition to describing the mechanism of enhancement, much of the early work in SERS was aimed at verifying that the signal measured was single-molecule in nature and once this was done, extract a meaningful interpretation of the results. This required one to locate the points of maximum enhancement on the SERS substrate at so-called, "hot-spots". These hot-spots would then need to be sufficiently small such that they contained only a single molecule. Finding these hot-spots is extremely challenging due to the required size. Furthermore, the acquired Raman spectra are highly sensitive to changes in their environment which, at the nanoscale, is in constant flux resulting in spectral "blinking" of Raman peaks making interpretation of results challenging[53].

To overcome the difficulties associated with verifying single-molecule Raman scattering, particularly in locating the hot-spots of SERS substrates, a novel approach using different scanning probe microscopies was introduced in which the probe of either an AFM[54] or STM[55] could be used to dynamically create hot-spots at the interface of the tip and substrate. This method, known as tip-enhanced Raman spectroscopy (TERS), works in a manner similar to SERS. By illuminating an ultra-sharp metallic tip several nanometers away from a SERS substrate, it is possible to excite localized surface plasmon-polaritons at both the substrate and the tip. If the gap is sufficiently small, the plasmons may hybridize, creating what are known as gap-plasmons. These gap-plasmons demonstrate remarkable enhancement and confine the electric field in an ultra-localized region (Figure 3-4a). This lightning rod effect makes the finding the location of hot-spots trivial and limits the number of molecules in the region. This has resulted in TERS being regarded as one of the most powerful analytic techniques. The utility of TERS measurements has been shown recently in the works of Lee *et al.* in which they combined methods in scanning near-field optical microscopy (SNOM), to directly image the vibrational modes of an isolated single-molecule[56]. In this work, the authors used the head of an ultra-sharp copper tip as a waveguide to focus an excitation source directly at the apex of the tip creating an even tighter confinement of the field. They were then able to scan over a copper surface containing an immobilized Co(III)-tetraphenyl porphyrin molecule. The high sensitivity of this technique allowed them to then map the intensity of the Raman scattering for different vibrational modes to generate an image with sub-nanometer resolution. Mappings of the different modes can be seen in figure 3-4.

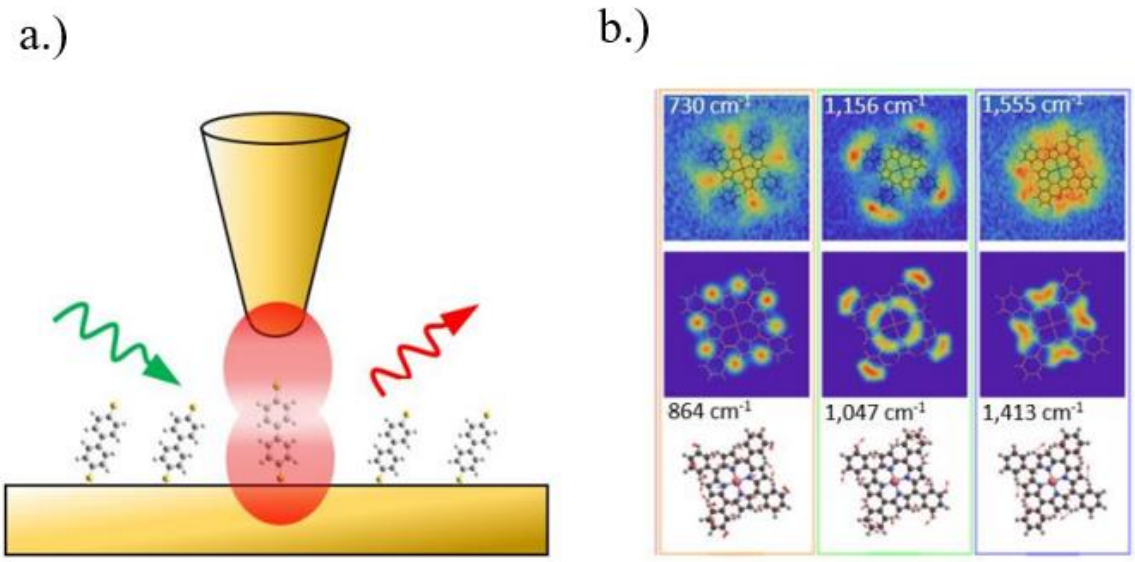

Fig. 3-4. (a) Illustration of the TERS effect in which surface plasmons created by an external excitation source hybridize with plasmons from the tip to create a significantly large electromagnetic field and subsequent intense Raman signal. (b) spatial Raman mapping of select vibrational modes of a single molecule measured using TERS[56].

3.4 Junction-Enhanced Raman and Conductance Spectroscopy

The most attractive prospect of single-molecule Raman spectroscopy is the ability to observe the dynamics of individual molecules under equilibrium conditions as well as their response to external perturbations. Such information can revolutionize the way we view fundamental chemical processes such as chemical reactions, catalysis, and protein folding and unfolding. Despite the rampant success Raman spectroscopy has experienced over the last few decades, it still suffers from several drawbacks, limiting its utility in everyday laboratory use and the pursuit of such endeavors. Imaging down to the single-molecule level requires the availability of extreme environmental conditions, such as ultrahigh vacuum and cryogenic temperatures, that can be integrated into a TERS system to provide stable measurement conditions, minimize contamination, and reduce signal fluctuations due to molecular reorientation.

One alternative approach to increasing the reliability of single-molecule measurements as well as provide the opportunity to measure the response of the system to various perturbations is to combine the capabilities of TERS with the techniques involving SM-BJ experiments discussed previously in chapter 2. The combination of these methods is a rare occurrence in physics and engineering in which two powerful techniques can be used together in a synergistic manner without detracting from the either's performance or capabilities. In one regard, the electrical data from SM-BJ experiments acts as a means of validating single-molecule spectral data when simultaneously measuring the Raman scattering at a hot-spot created by the tip-molecule-substrate junction. Additionally, it offers the opportunity to directly observe the structural response of a single-molecule system under the influence of external sources.

The first attempts to demonstrate the successful measurement of Raman scattering from single-molecules in break junctions in 2006 by Tian *et al*[10]. In this work, the authors made use of a MCBJ system to measure the Raman response of 1,4-benzendithiol molecules at the junction at different separation distances of the electrodes. A depiction of this experiment can be seen in figure 3-5a where the intensity of the Raman scattering from the molecule is shown to increase as the size of the gap is reduced as a result of the formation of gap plasmons. They then showed that the maximum enhancement occurred at the apex of each end of the junction and showed that the degree of enhancement is polarization dependent. This claim of polarization dependence is necessary for supporting their claim that the enhancement is a result of the gap because it is well established that the coupling of the excitation source to the cavity of nanostructures displays this dependence. In the case of perpendicular polarization, the excitation field was only weakly coupled to the nano-gap as it was no longer aligned with the surface fields, whereas the opposite case of parallel polarization displayed strong coupling and thus enhancement of the Raman scattered light.

Although conductance measurements were not done as a part of this work, it's contribution is invaluable for demonstrating the possibility for integrating field enhanced Raman measurements with standard break junction techniques for study transport phenomenon in single-molecule systems.

This work was expanded upon shortly thereafter by Ward *et al.* who demonstrated the combined measurement of Raman spectrum and conductivity in electromigrated single-molecule junctions [11]. This was done by simultaneously measuring the junction current with the enhanced Raman signal in time which allowed them to see correlated changes in the Raman spectra with changes in the conductance with spectral features drifting as far as 20 cm^{-1}. This behavior is displayed in figure 3-5b. Their claim of enhancement from the junction was further supported by observed fluctuations in the Raman intensity which are characteristic of field enhanced Raman scattering. The presence of these fluctuations in the Raman signal makes interpretation of Raman spectra tremendously difficult as it becomes nearly impossible to compare spectral features between individual spectra and validate that the spectra is originating from a single molecule or from a contaminant. One proposed mechanism for these fluctuations is the stochastic reorientation of the individual molecule the Raman signal is originating from [53]. Raman scattering is governed by the symmetry of the vibrational modes of the molecule and is rarely isotropic. Thus, even minor variation in the configuration of the molecule relative to the local electric field may result in dramatic changes to observed spectral features. When measured with sufficiently short integration times, it is possible to gain deep insight into the dynamics of the single-molecule system as well as the distribution of the inhomogeneous electric field within the gap.

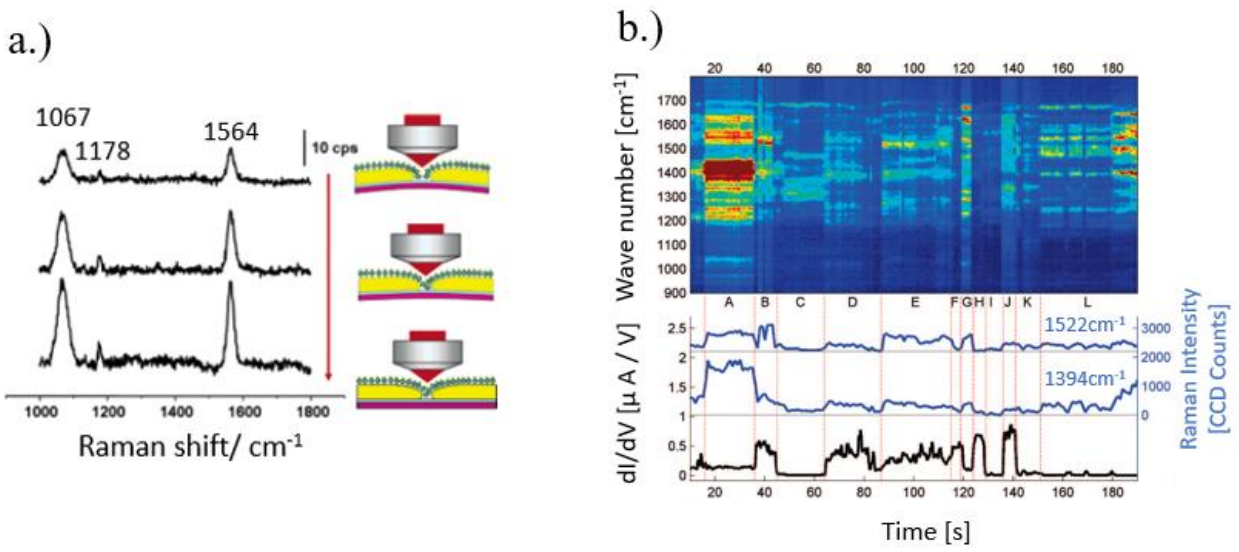

Fig. 3-5. Combined TERS and Conductance experiments. (a) First demonstration of enhanced Raman from a break junction setup[10]. (b) Time correlated measurements of enhanced Raman scattering and electrical measurements in a break junction system[11].

This work demonstrates the true potential of combined field enhanced Raman and conductance studies. Furthermore, the results reported in this work were acquired under ambient conditions which demonstrates the possibility for studying molecular systems in environments that are easily accessible to the scientific community. Since their initial publication, several other impressive works on the Raman response of single-molecule junctions have been demonstrated improved techniques for collecting combined Raman and conductance data[12], [57] to investigations of effects of gating on the Raman response of single-molecule junctions[58] and local heating of single molecules[59]. While these works have reported highly impressive results, advancement in this area is still ultimately hindered by long integration times which average out the dynamics of the molecular junction or the lack of a rigorous statistical analysis that allows for the validation of single-molecule sensitivity and a clearer understanding of the otherwise complicated single-molecule Raman spectral data. Thus, by addressing these issues it would then

be possible to gain substantial information on the intricacies of single-molecule junctions and expand these capabilities to other branches of the scientific community.

CHAPTER 4

Junction Enhanced Raman and Conductance Spectroscopy (JERCS) System Design

4.1 Introduction

To investigate the relationship between molecular structure and transport properties in single-molecule systems, it was necessary to develop an experimental platform that can characterize each domain independently and cooperatively to extract mutually verifiable information on the junction dynamics in real time. Based on the discussion of break-junction characterization methods and TERS in the previous chapters, it can be seen that these two independent techniques may be combined in a seemingly symbiotic way and without diminishing their individual performance. To this end, we developed a laterally oriented STM-BJ system which was then combined with a commercially purchased confocal Raman microscope and spectrometer to independently and simultaneously characterize the conductance and Raman response of a self-assembled monolayer (SAM) of 4-4'-biphenyldithiol (BPDT) formed on a gold substrate. The STM-BJ apparatus was first developed with consideration to the spatial restrictions of the confocal microscope and preliminary conductance measurements were performed on a SAM of BPDT and compared against values reported in the literature for validation. Verification of field enhancement due to the tip in close proximity of the surface was performed and the resultant spectra was compared against simulated Raman spectra determined from density functional theory (DFT) calculations. Upon validation of performance in both domains, combined conductance and Raman measurements were performed in which correlated changes in the conductance, known as blinks, indicating the formation of a molecular junction could be observed. These subsequent blinking events were

directly correlated with dramatic changes in the Raman intensity of BPDT suggesting that the resultant spectra originated from a single molecule as opposed to the background ensemble.

4.2 Design of JERCS System

As discussed in chapter 2, there are several methods for performing conductance measurements which may be combined with Raman spectroscopy. MCBJs are laterally oriented which are suitable for placement under a microscope objective, however the deformation of the substrate necessary to create and break junctions moves the point of junction formation in and out of the microscopes focal plane which reduces the efficiency of collecting Raman scattered light. Alternatively, vertically oriented configurations based on STM-BJ systems have also been used for Raman through the use of special tips that are fabricated to act as the contact electrode as well as a waveguide for the excitation source. This ensures that the point of junction formation is also the hotspot for TERS activity. While this approach makes finding the hotspot trivial, fabrication of the tip and system design is much more complicated.

With this in mind, we opted to implement a laterally oriented STM-BJ system in conjunction with an optical setup. While less mechanically stable than a MCBJ or vertically oriented STM-BJ, it offers the advantages of high collection efficiency, due to a stable focal plane and less required optics and is substantially easier to implement then it's vertical counterpart with a commercially purchased confocal Raman microscope. With this approach, the electrical characterization system may be used in dependently or combined with the Raman spectroscopic system. A block diagram illustrating the general system design may be seen in figure 4-1.

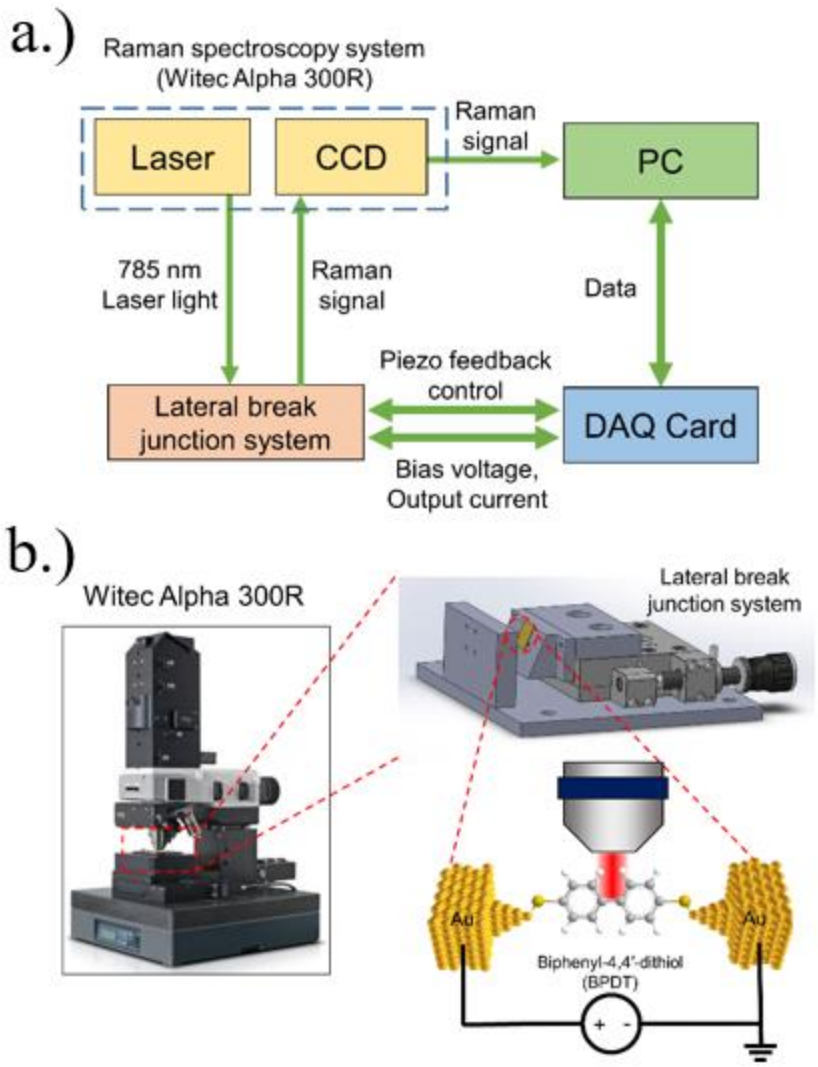

Fig. 4-1. (a) Block diagram of JERCS system and (b) depiction of the optical and electrical components included in the design.

4.2.1 Design and Testing of Lateral STM-BJ System

The laterally oriented STM-BJ system consisted of an optical stage controlled by a differential micrometer (Thorlabs, model name LNR25D) for mounting and biasing a gold substrate which acts as the sample platform for forming SAMs to be used during an experiment. Facing opposite the optical stage was an aluminum wall supporting a piezoelectric block (Thorlabs, model name: PA4GEW, 2.2 µm displacement at maximum 150 V piezo voltage) and a

cylindrical steel tip-holder for current sensing. The differential micrometer was used as a means of coarse control to bring the substrate within range of an electrochemically etched gold tip mounted within the steel tube such that a tunneling current could be detected over the length of the tip-substrate gap. Once this distance was achieved, the piezoelectric block would be used for fine control of the tip-substrate gap distance in either an open or closed loop configuration via a LabView graphic user interface depending on the type of measurement being performed. A real image of the laterally oriented STM-BJ system can be seen below in figure 4-2.

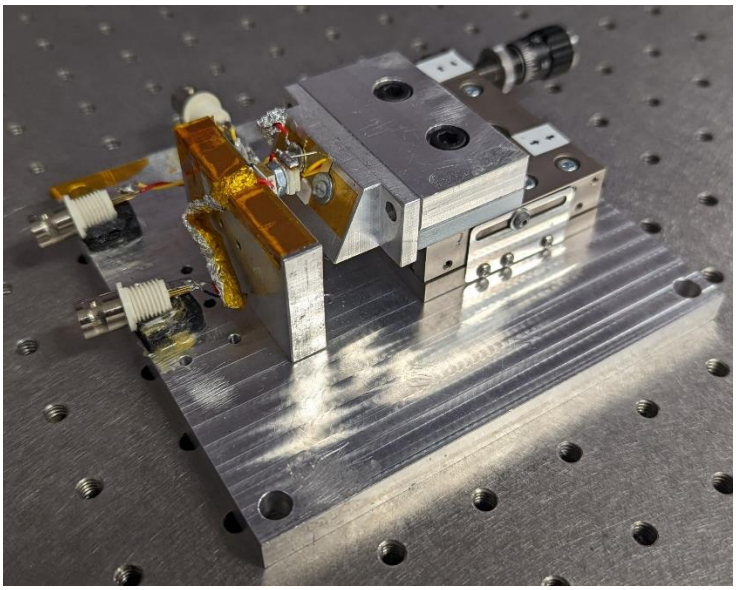

Fig. 4-2. Image of laterally oriented STM-BJ system.

To successfully perform electrical characterization or TERS measurements, an ultrasharp conductive tip is necessary to physically contact molecules or dynamically form highly localized plasmonic hot spots. To satisfy these requirements, tips were prepared by electrochemically etching 0.25 mm thick gold wire (Alfa Aesar, 99.998%) using a modified version of the methods outlined in reference [60]. This method utilized a 1:1 solution of hydrochloric acid (~37% weight concentration, Fisher Scientific) with pure ethanol (200 proof, Sigma Aldrich) as the working

electrolyte solution. The anode used in this process consisted of gold ring, approximately 1 cm in diameter, made from winding the same gold wire as the STM tips. The anode was gently placed on the surface of the electrolyte solution until a meniscus could be seen forming between the ring and the solution. The gold wire, acting as the cathode electrode, was partially submerged in the solution at the center of the ring and oriented perpendicular to the surface of the solution to ensure uniform etching. After placing the anode at the surface of the solution and submerging the cathode, a DC bias of ~2.4 V was applied to the electrodes and the current was monitored. At this point, small bubbles could be seen to form, and the solution slowly began to change color, indicating that the etching process was underway. When current flow through the system could no longer be measured, it could be seen that the submerged portion of the wire was separated from the wire above the surface of the solution, leaving a sharp conical tip at the apex of the wire. The opposite end of the tip cut to a length of ~0.5 cm to be later mounted in the steel-tube of the STM-BJ system. After shortening the tip, residue from the electrolyte solution was removed by immersing the tip in deionized water and subsequently drying it using a gently N_2 stream. After cleaning, the etched tips were stored under vacuum until they were needed for any measurements. Through this etching process, tips with a radius of curvature smaller than ~200 nm could be achieved regularly. Figure 4-3 below shows a scanning electron microscope (SEM) image of an electrochemically etched gold tip made from this process.

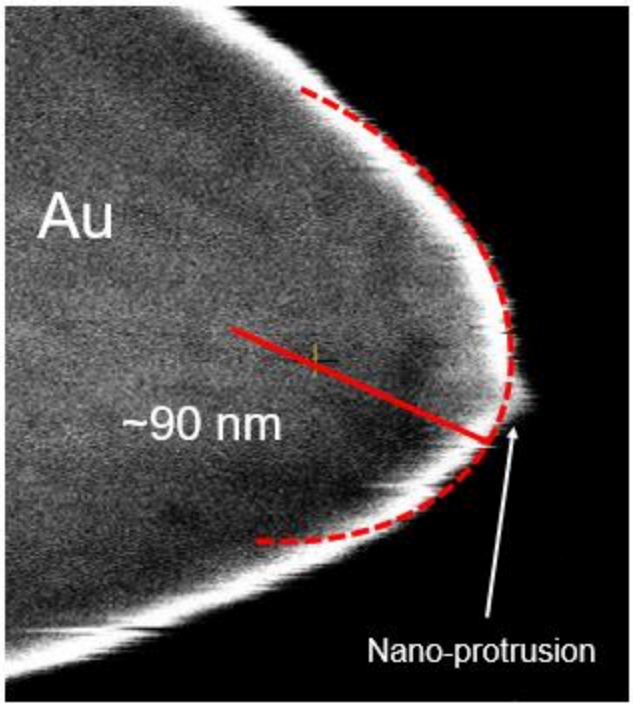

Fig. 4-3. SEM Image of electrochemically etched gold tip. This tip has a measured radius of curvature of ~90 nm as well as an irregular nano-protrusion that functions as the contact point for junction formation.

While this process produces tips that appear uniform under a microscope, a closer examination shows that nano-protrusions may form at the apex of the tip which act as the actual contact point of the molecular junction and location of hot-spot formation in TERS.

Validation of the electrical characterization portion of the system was done by performing tapping measurements (discussed in chapter 2) to repeatedly measure and statistically verify the conductance of a target molecule. For this purpose, we chose BPDT as it is a model molecular system whose electrical properties have been previously reported [61] at the single molecule level allowing us to compare our results.

Sample substrates of gold were prepared by evaporating ~130 nm of gold onto a mica substrate which were subsequently cut into 1 cm by 1 cm squares prior to being stored under vacuum. Before using the substrate for SAM formation, it was flame annealed for ~10 seconds

using a butane torch. The SAM was formed at the surface of the gold by immersing the substrate in a 1 mM solution of BPDT (Sigma Aldrich, 95%) in tetrahydrofuran (THF, Sigma Aldrich, ≥ 99.0%) for approximately 18 hours to allow for monolayer formation. Following incubation, the substrate was removed from the BPDT solution, rinsed with pure THF, and dried with a N_2 stream.

Tapping measurements were then performed on the BPDT reference system. During initial testing, 5,032 current vs. distance tapping traces were collected at an applied bias voltage of 50 mV. The measured current was then amplified and represented as a voltage for the data acquisition system to read using a 10 nA/V transimpedance amplifier. During this process LabView was used for both control of the piezoelectric block and data acquisition. An automated algorithm was then used to select curves containing a conductance plateau, indicative of the characteristic conductance of a molecular junction, in a given trace. This algorithm works by first taking the residual of a line fit to each trace in semilog scale and comparing it to the value of a simple tunneling decay. If the residual is over a typical cutoff value (in this case 0.5), i.e. the trace cannot be fit to the decaying tunneling current due to the possible formation of a conductance plateau, the algorithm will construct a histogram of the conductance values from a single trace. If the number of counts in any single bin exceeded a defined threshold value, suggesting a stable plateau in the current, then the current was considered to represent the conductance of a single molecule and stored in memory to form a cumulative distribution of conductance values which could be used to statistically determine the conductance distribution of the molecule under study. Figure 4-4a depicts example selected single traces from the preliminary measurements of the BPDT reference system. In this instance, the threshold for bin counts was 7 which resulted in the selection of 461 out of 5,032 individual tapping traces which were then used to construct the total histogram for the conductance of BPDT shown in figure 4-4b. The distribution of this histogram displays a sharp peak centered

at ~6.5x10^{-3}G$_0$, where G$_0$ is the quantum of conductance discussed previously in chapter 2 ($2e^2/\hbar$). The characteristic conductance for BPDT in these measurements is agreeable with previously reported results on this molecule[61] thus allowing us to validate the performance of the electrical characterization component of the JERCS system.

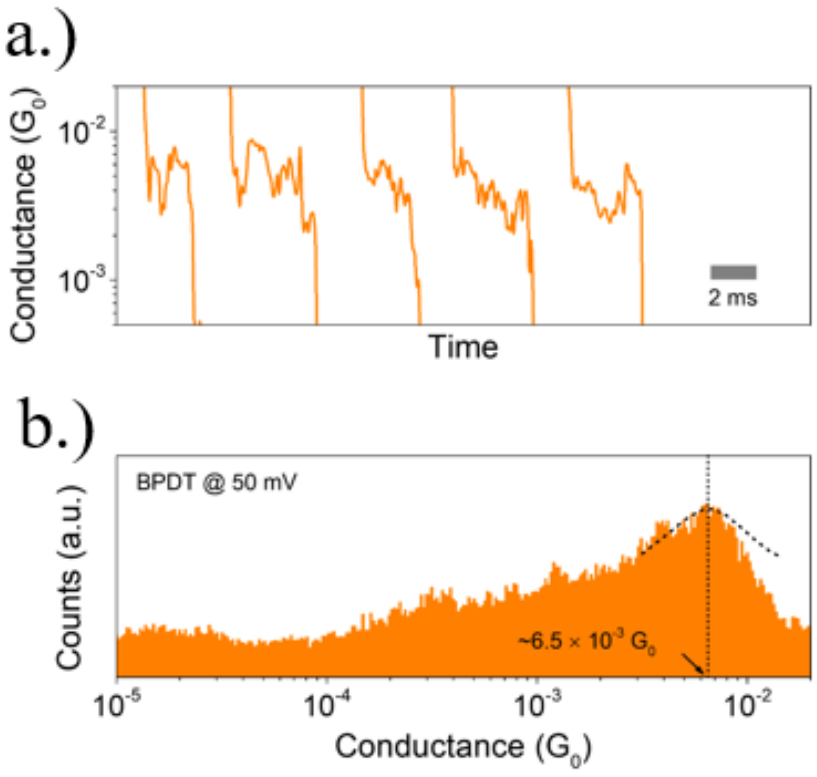

Fig. 4-4. (a) Select individual conductance versus time traces from BPDT tapping measurements. (b) Conductance histogram of all selected traces from the BPDT tapping measurements. The peak of this distribution is taken to be the characteristic conductance of BPDT.

4.2.2 Overview of Optical System

The optical component of the TERS system consisted of a commercially purchased confocal Raman microscope and spectrometer (WiTec Alpha 300R) fiber coupled to 785 nm diode laser (Topica XTRA II) which acted as the Raman excitation source. The laser was focused at a desired location using a 100x objective lens with a 0.75 NA and 4.1 mm working distance (Zeiss, model name: 100x LD EC Epiplan-NEOFLUAR) which also acted as the collection optics for the

Raman scattered light. The objective height and sample positioning was controlled using software provided by the manufacturer (WiTec, Control 5.0 software suite) while reading and handling of data was done using a custom LabView interface which also controlled the electrical characterization system.

Preliminary reference measurements of the BPDT system were taken to verify enhancement of the Raman scattering due to the presence of the tip gently contacting the gold surfaces. This process can result in the trapping of many molecules between the tip apex and substrate and can result in a notably large enhancement of the Raman signal. Figure 4-5 shows an optical image of an electrochemically etched gold tip, lightly contacting the surface of a gold substrate supporting a SAM of BPDT along with a Raman map of the same area mapped according to the Raman intensity of the most prominent peak of BPDT spectrum located at 1597.4 cm^{-1} (v(8a) ring vibration mode).

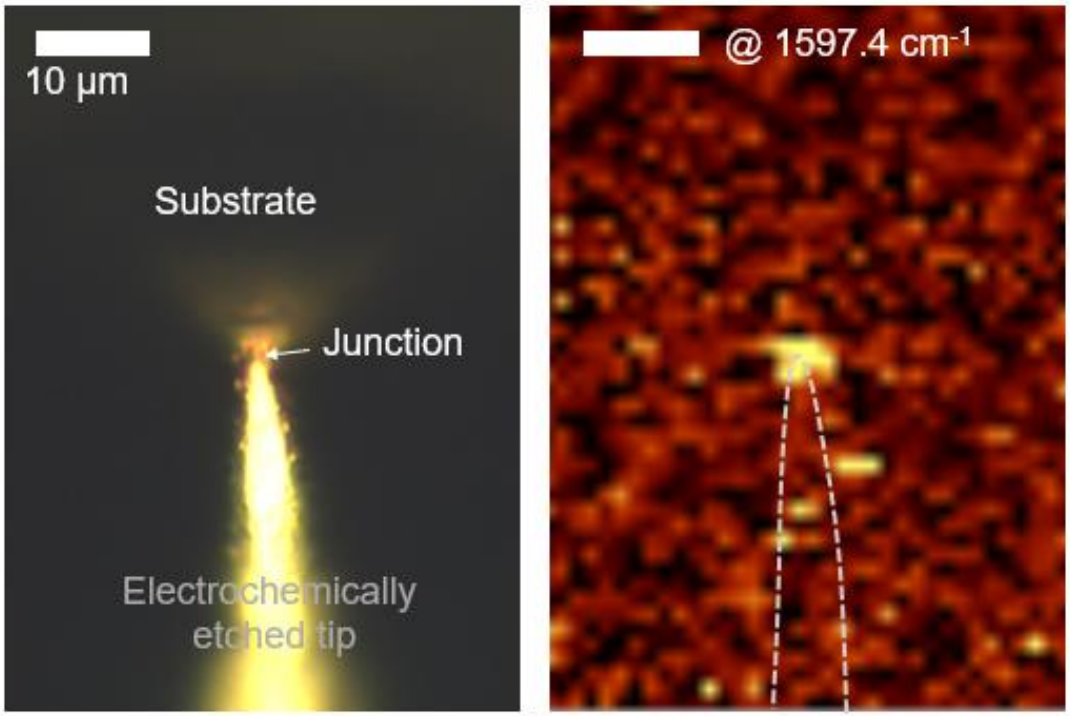

Fig. 4-5. Optical image (left) of an electrochemically etched gold tip in light contact with a SAM of BPDT formed on a gold substrate. Mapping of the Raman intensity of the primary breathing mode of BPDT centered at 1597.4 cm^{-1}. The intensity of the peak is highest near the contact point between the tip and substrate.

In this instance, the Raman mapping was acquired using an integration time of 22 ms with a single acquisition at an incident laser power of 5 mW. When in contact with the surface, a dramatic increase in the Raman scattering can be seen around the tip-substrate interface confirming the enhancement properties characteristic of TERS.

4.3 Combined Raman and Conductance Measurements

Upon preliminary verification of independent operation of Raman enhancement and conductance measurements, we wished to demonstrate the feasibility of the system by performing simultaneous measurement of the Raman response and conductivity by forming single-molecule junctions on a SAM of BPDT molecules formed on a rough gold surface. To do this, the substrate supporting the BPDT SAM was manually brought within tunneling distance of an ultra-sharp

electrochemically etched gold tip using a differential screw attached to an optical stage. Once a tunneling current could be observed, a piezo was used to control finely control the distance between the substrate and the tip. The piezo was to engage the tip towards the substrate until a setpoint value for the current could be measured at which point, feedback from the system would be turned off and stochastic jumps in the current would begin to appear which are indicative of a molecule intermittently binding between the two electrodes in so-called “blinking” events. The abrupt change in current during the blinking events can be seen in the lower panel of figure 4-6a with the corresponding Raman signal in the top panel. In this figure, the step heights of the blinks correspond roughly to the conductance value predicted previously in figure 4-4b suggesting that the recorded conductance values are the result of a single-molecule junction forming. In the case of the JERCS system, we also observe a correlation in the intensity of the Raman signal in both the Stokes (positive region) and anti-Stokes (negative region) while a molecular junction is formed. Once the junction breaks down (as evidenced by the abrupt decrease in conductance) the Raman intensity also drops off. The relationship between the junction formation and Raman intensity is due to two contributions which have been discussed previously, namely the electromagnetic enhancement within the cavity formed by the tip and substrate and the chemical enhancement due to the change in the polarizability of the bonds from the molecule binding to the leads. These leads to a distinction between junction enhancement and traditional TERS in which no junction is formed.

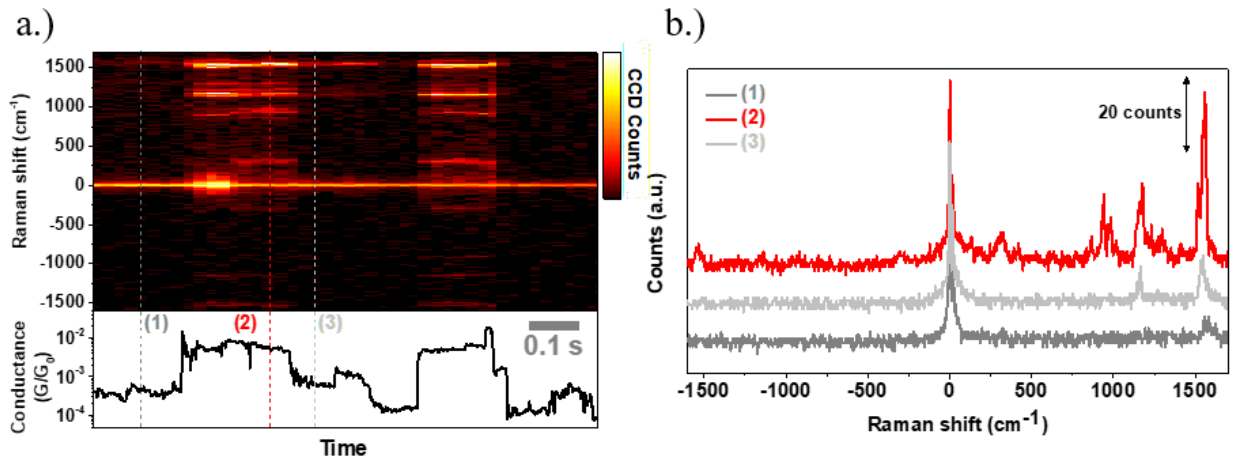

Fig. 4-6. (a) Single molecule blinking events showing correlated Raman (top panel) and conductance (bottom panel) signals suggestive of single-molecule measurements. (b) Single-molecule Raman spectra of BPDT recorded at three separate times highlighted in (a).

The single-molecule nature of these measurements are further supported by the large spectral intensity of peaks in the anti-Stokes region at high energies (~-190 meV). As stated previously in chapter 3, anti-Stokes lines appear due to a mode being in a vibrationally excited state. When a bias is applied to a molecule, a small portion of the tunneling electrons transmit inelastically through the junction and exchange energy with the vibrational modes which can increase the amount of anti-Stokes scattered photons. In the figure 4-6, this increase in anti-Stokes scattered light only occurs during blinking events in which a molecule is present in the junction and thus can't be attributed to optical pumping of the vibrational modes.

To substantiate this hypothesis, we performed a series of blinking measurements at different bias voltages to observe the ratio of Stokes to anti-Stokes peak intensity. The results of these measurements can be seen in figure 4-7.

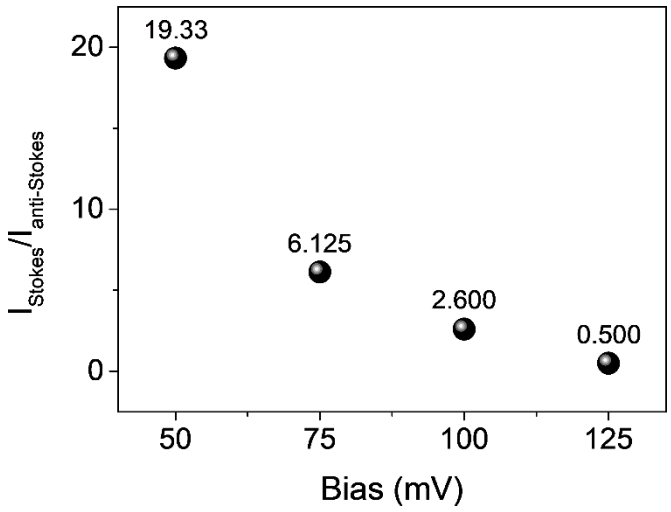

Fig. 4-7. Ratio of Stokes to anti-Stokes intensities for the primary vibrational mode of BPDT as a function of applied bias.

From this figure, we can see a notable decrease in the ratio of Stokes scattered light to anti-Stokes scattered light as the bias voltage is increased. This suggests that higher energy electrons are in fact exchanging energy with the system supporting out previous claim that the increase in anti-Stokes scattering is the result of transporting electrons and not optical pumping and therefore the Raman signal must be originating from a single molecule.

4.4 Conclusion

In this work, we developed an experimental apparatus capable of measuring the conductance and Raman scattering of a molecular system simultaneously and independently. Single molecule resolution was verified through observations of correlated behavior in the conductance and Raman intensities that occurred explicitly during the formation of a molecular junction. The nature of this observation was further supported by the increase in intensity of peaks in the anti-Stokes region of the Raman spectra. The dependence of the ratio of Stokes scattering

intensity with anti-Stokes scattering intensity as the bias voltage is varied suggests that the change in anti-Stokes intensity originates from electron-phonon interactions due to current flowing through the junction and not from optical pumping, which further supports our claim that the Raman scattering signal originates from a single molecule. The successful development of the JERCS system and validation of its ability to reliably detect single molecules allows for the exploration of the dynamics of chemical systems in both the fields of molecular electronics as well as chemical science in general. Using this technology, it is possible to explore in finer detail, the dynamic structural behavior that influences charge transport in single molecules such as changes in internal degrees of freedom or direct observation of binding configurations thought to be one of the main factors responsible for the dramatic variation in the conductance of these systems.

CHAPTER 5

Identifying Dynamic Structural Behavior in Single-Molecule Junctions

5.1 Introduction

After developing a system capable of simultaneously measuring the conductance and Raman response of a molecular system with single-molecule sensitivity, we next wished to perform a deeper investigation on the statistical behavior of these junctions and model their dynamic behavior over the course of a blinking event. In this chapter, we investigate the statistical behavior of the Raman spectral data acquired during blinking measurements using the JERCS system developed in the previous chapter to differentiate between spectral data from a single molecule of BPDT and spectra from the background molecular ensemble. This is done by leveraging machine learning algorithms, specifically k-means clustering, allowing us to produce a representative spectrum for each cluster as well as classify the spectral data in time as single-molecule or not. This allows us to reliably identify single-molecule conductance and Raman events for further investigation. A comparison of the representative spectrum from each cluster revealed a red shift in the peak position of the main Raman peak corresponding to the ring breathing mode of BPDT during the formation of a molecular junction when compared to the Raman spectrum of the background ensemble. This behavior suggests a tensile strain is present in the bound molecule compared to its unconstrained variation. This phenomenon was investigated further by analyzing the evolution of the conductance and peak position of the Raman mode in question over the duration of a blinking events. This analysis showed that a decrease in Raman shift corresponded to a direct increase in conductance. The Raman peak position measured during the blinking event was then used to model the structure of BPDT under an applied strain and as well as it's coupling

to the junction allowing us to paint a clear picture of the dynamic behavior of the molecular junction and its transport properties. These results demonstrate that the JERCS platform developed in this work is capable of providing deep insight into how changes in the internal structure of a molecule can affect its transport properties.

5.2 Experimental Results

To develop a deeper understanding of how structural changes in BPDT influenced its electron transport properties, we performed blinking measurements in the same manner as the previous chapter to develop a cumulative data set for the purpose of statistical analysis. From these measurements, 10,955 spectral data points were selected by manually searching for occurrences of blinking events in the conductance data that was directly correlated with an increase in the intensity of the Raman bands. When manually selecting data, an equal amount of data was taken before and after the step-like feature in the conductance data such that a comparison between spectral features could be made when a junction was formed and when it wasn't.

To determine if specific modes or spectral features could be used to clearly identify when a single-molecule spectra/junction is obtained, we turned to an unsupervised machine learning approach to establish a statistically significant "fingerprint" for junction formation. Here, we focus on clustering the 1200-1700 cm^{-1} region of the Raman spectrum from the manually selected data. The corresponding conductance data is not provided to the algorithm, so this information can be used to verify that the spectral features correspond to when a single-molecule junction is formed between two electrodes. Intensity plots of the spectral data in this region were grouped through k-means clustering (Figure 5-1, top) into 2 clusters to separate single-molecule events and background spectra. The two clusters show drastic differences in their spectral features. Spectral

lines in the first cluster (denoted as “On Cluster”) have notably higher intensities and greater variation that the other cluster (“Off Cluster”) which is significantly lower in intensity. A histogram of the conductance corresponding to the measured spectrum in each cluster (Figure 5-1, bottom) shows a sharp distribution centered at the characteristic conductance of BPDT ($6.5 \times 10^{-3} G_0$) for the On Cluster while the histogram for the Off Cluster shows a distribution with a much wider breadth centered at a lower conductance value near the setpoint current for the measurements. It is important to note that these statistical results match the observations from the single-molecule case above. In cases where the conductance matches the characteristic conductance of BPDT (i.e. a junction is formed) there are significant increases in intensity across the spectral region. The outcome of this analysis implies two important capabilities for single-molecule JERCS measurements. First, it allows us to identify spectral features that are representative of the formation of a single-molecule junction and to analyze changes in molecular configuration vs. idealized structures. And second, it enables us to process a large amount of recorded data to find long lasting blinking events with correlated spectral and conductance features. The information contained in these measurements allows us to analyze dynamic processes that occur within the single-molecule junction and provides an opportunity to understand the changing mechanics of these systems and how structure relates directly to the properties of single-molecule systems such as electron transport.

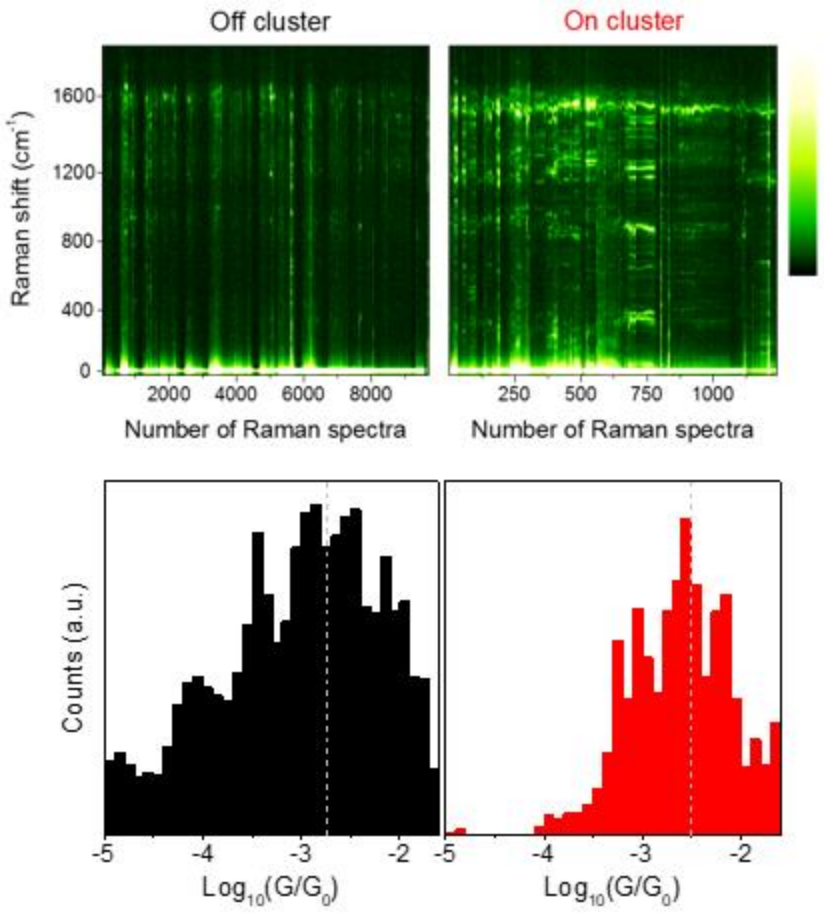

Fig. 5-1. Set of collected spectra assigned to each cluster by k-means clustering (top panel) and associated conductance distributions for each cluster (bottom panel).

5.3 Theoretical Analysis and Discussion

To determine specific spectral features, we use the average spectra of each cluster (Figure 5-2), and density functional theory (DFT) calculations of the molecule in-contact and out-of-contact as our basis for comparison. There are several prominent features present in the On Cluster data that are not apparent in the Off Cluster data such as the ν(6a) mode at ~350 cm^{-1}, and the ν(17b) mode at ~800 cm^{-1}. However, the vibrational mode related to the ν(8a) ring vibration is the most prominent and is clear in both clusters. This mode shows a dramatic shift in frequency from 1594 cm^{-1} (Off Cluster) to 1540 cm^{-1} (On Cluster). The DFT simulations of model geometries for

each cluster show a similar trend, shifting from 1588 cm^{-1} off contact to 1572 cm^{-1} in the on-contact geometry. We also note that the width of the averaged spectrum for this mode is significantly broader than in the individual single-molecule spectra, suggesting significant fluctuations in this mode depending on the junction geometry. Therefore, the combined changes in vibrational energy and intensity between the on and off states suggest that this mode can be used directly as a spectral-feature of interest to study.

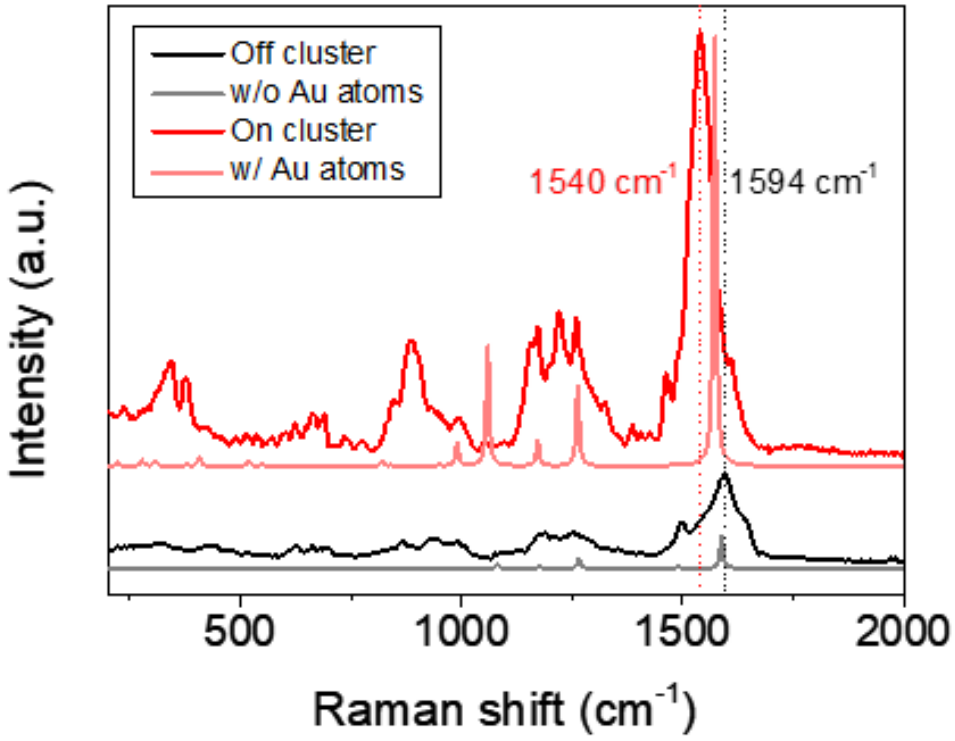

Fig. 5-2. Average spectra and theory comparison of BPDT for On Cluster data (red) and Off Cluster data (black).

Thus, by utilizing the insights gained above from the statistical analysis we identify a junction from the "On Cluster" as shown in figure 5-3 that displays a clear blinking event correlated with an increased intensity of the Raman spectrum, and a decrease in the ν(8a) ring vibration mode energy. As can be seen in figure 5-3, this mode changes over a range of 1565-1585

cm^{-1}, over the time the junction is held, and the changes in this mode frequency are well correlated with *specific* features of the conductance trace. As this is a break-junction system, the electrodes are not perfectly stable, but instead tend to drift with time, inducing either a compressive or tensile strain on a bound molecule. While the drift is a stochastic random walk, the electrodes tend to be drifting apart during the measurement of this junction. During the first part of the blink (green dots), the conductance slightly increases possibly due to the planarization of the phenyl rings as the junction is stretched. Additionally, a corresponding decrease in the Raman shift of the ν(8a) mode can be seen with increasing tensile on junction. At ~0.166 s there is a sharp, stepwise decrease in the conductance. This discontinuity is accompanied by a simultaneous increase in the ν(8a) frequency, corresponding to a relaxation of the molecular junction, and is likely due to a change in the gold configuration of the electrodes. From this point, there is again a systematic increase in the conductance and decrease in the ν(8a) ring vibration frequency (brown dots) as the junction is strained until its eventual breakdown at ~0.375 s.

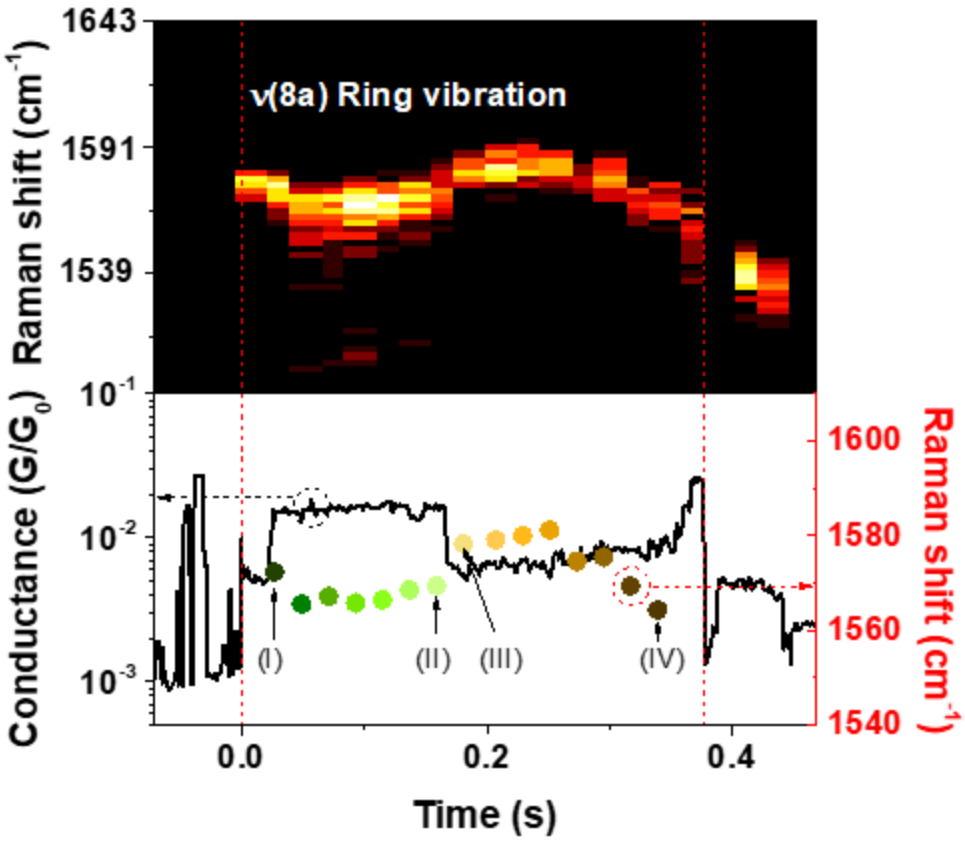

Fig. 5-3. Correlated Raman spectra showing only the main ring vibration (top panel) with it's corresponding conductance trace (bottom panel). Peak positions of the main vibrational model are depicted further in the conductance trace and are colored green and brown according to two apparent conductance distributions present.

To substantiate our hypothesis that the correlated variation in the conductance and Raman shift are the result of a tensile strain in the junction, we performed DFT and Green's functions-based transport calculations to model the Raman spectra conductance properties of a BPDT molecular junction subjected to mechanically induced tensile strain. The junction was modeled as a BPDT molecule with a single Au atom bound to each thiol group. The strain on the system was simulated by increasing the Au-to-Au separation distance and relaxing the molecule prior to calculating the Raman spectrum and zero-bias conductance. Relaxation of the molecular system, and subsequent vibrational and electronic structure calculations were performed using the

Gaussian09 software package[62]. DFT calculations were performed using the B3LYP density functional with the 6-31g(d,p) basis set for the organic atoms and the LANL2DZ basis set with effective core potential was used for the gold atoms. NEGF calculations were then carried out on the relaxed structures to model the transmission functions and zero-bias conductance values using a modified version of the MolTran, Molecular Transport code, originally developed by Hashem Mohammad and M.P. Anantram from the University of Washington Comotion[63]. For these simulations, the coupling of the molecular junction to the electrodes (Γ) was used as a fitting parameter to model the conductance of the experimental data to theoretical structures whose ν(8a) mode frequency matches the experimental data. The zero-bias conductance was then calculated as the value of the transmission function at the fermi level which is taken to be the work function of gold (-5.1 eV). The theoretical relationship between conductance and Raman shift can be seen in figure 5-4a while the calculated transmission functions can be seen in figure 5-4b. As tensile strain on the junction increases, the Raman peak associated with the ν(8a) mode decreases while the zero-bias conductance increases which is in direct agreement with our experimental results. By using the coupling to the terminal gold atoms (Γ) as a fitting parameter, we were able to accurately model two distinct trends which can be seen in figure 5-5. Each population of the acquired data points in figure 5-5 follows these increasing trends which indicates a tip drift-induced tensile strain was applied to the molecular junction. Additionally, this suggests that the discontinuity in experimental results is related to sudden change in coupling suggesting a reorganization of the Au atoms at the metal-molecule interface.

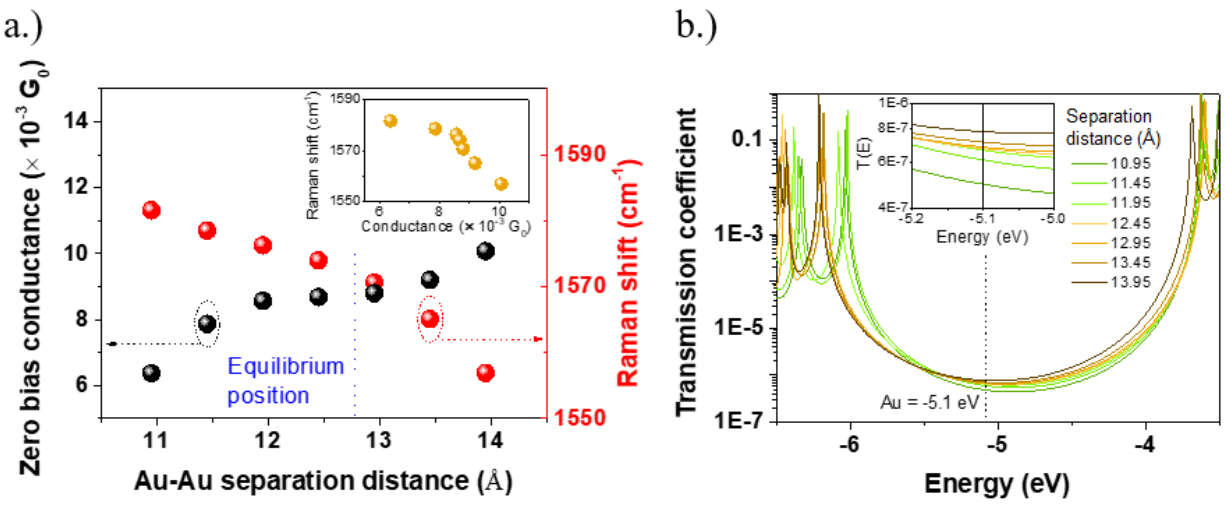

Fig. 5-4. (a) Simulation of Raman Shift of main breathing mode and zero-bias conductance of BPDT molecular junctions under strain. A plot of the Raman shift against the conductance for each configuration (inset) shows a clear negative correlation between these features. (b) Transmission plots for each configuration. The zero-bias conductance is taken to be the value of the transmission at the fermi-level which is treated to be the work function for gold (-5.1 eV).

By fitting the calculated Raman shift of the ν(8a) mode and conductance from our model system to the experimental data shown in figure 5-5 we were able to visualize the dynamics of the junction throughout the blinking event. Figure 5-5 (points I through IV) illustrates the proposed changes in the junction configuration over time. Following the formation of the molecular junction (I) the molecule is subjected to tensile strain resulting in a slight increase in the length (II). At the point of discontinuity, the molecule experiences a sudden reorganization at the interface which changes the coupling and effectively compresses the molecule (III). Elongation of the junction then continues until the junction breaks down after point IV. These results indicate that the variation in the conductance and the Raman shift is due to a mechanically induced strain, in accordance with our experimental results.

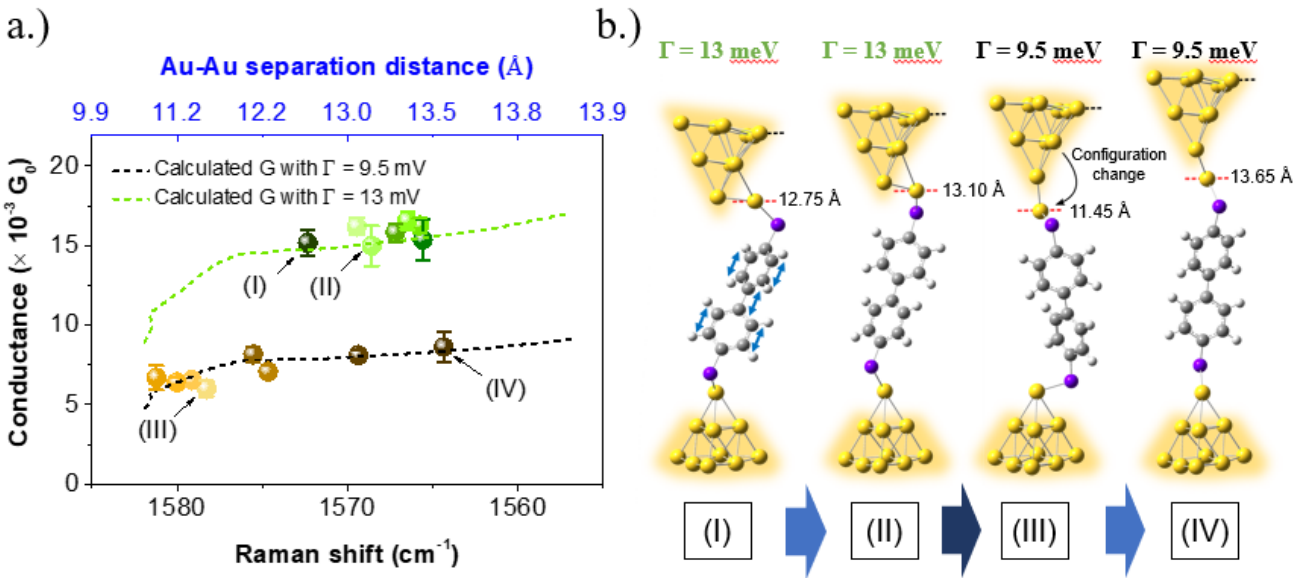

Fig. 5-5. (a) Simulated Raman shift of primary breathing mode and conductance values of BPDT junctions under mechanical strain. (b) Model structures theoretically mapped from the experimental data illustrating the trajectory of the junction over time.

5.4 Conclusion

In conclusion, this multi-dimensional spectroscopic platform allows simultaneous measurement of the structural, mechanical, and electronic transport properties of a single molecule. By performing combined single-molecule, high temporal resolution, Raman spectroscopy with molecular transport measurements *in situ*, we can extract information concerning the configuration and dynamics of the molecule within the junction under ambient conditions. The combination of time correlated changes in molecular conductance measurements with Raman signatures in both the Stokes and anti-Stokes regions, statistical measurements of changes in the spectra and specific modes when a molecule is bound between two electrodes, and the shifts within modes during these events allow for direct insights into the evolution and modulation of a single-molecule. The high-speed nature of the measurements allows for the acquisition of large quantities of data necessary for performing a statistical analysis using unsupervised machine learning. This analysis acts to verify the integrity of these measurements and to isolate characteristic data sets possessing

physically significant features. Thus, this combined JERCS system provides a versatile and accessible platform for the continued investigation of chemical processes at the single-molecule level which could allow insights into a variety of chemical and biological processes including field driven chemical reactions, enzymatic processes, and molecular binding and transport processes.

CHAPTER 6

Examining Binding Configurations in Cysteine Molecular Junctions

6.1 Introduction

Understanding of molecular structure and its relationship to charge transport can be loosely broken down into three separate problems, namely, the influence of the chemical structure of the molecular backbone, the effect of side groups, and the interaction of the anchoring group with the electrode at the molecule-metal interface. The exact nature of the metal-molecule interface and its impact on transport properties is a particularly important question that been studied extensively in previous works[61], [64], [65]. These efforts are largely pursued via systematic studies on select chemical structures to infer the influence of the metal-molecule interface on transport properties. With the exception of inelastic-tunneling spectroscopy (IETS)[39], none of these methods directly interrogate the chemical structure of the conducting molecule. Furthermore, the lack of rigorous selection rules in IETS[66], [67] makes interpreting spectral data ambiguous at best. Thus, there is a clear and evident need for a deeper analysis of the effects of binding configurations of single-molecule junctions on conductance that is supported by information from both transport and structural data.

In this chapter, we investigate the effects of chemical structure on electron transport properties, particularly binding configuration, in cysteine molecular junctions using the methods discussed in previous chapters. By collecting hundreds of Raman spectra with their associated conductance values from JERCS blinking events, it was possible to observe multiple conductance distributions in cysteine indicative of different binding configurations. Theoretical models were then used in conjunction with models developed from machine learning methods on the

experimental data to determine defining features in the Raman spectral data. This ultimately allowed for the determination of the molecular geometry within the junction and how its configuration affected its conductivity.

6.2 Cysteine JERCS Measurements

For this study, cysteine was chosen as the model system because it possesses several attractive qualities: (1) it is particularly significant in chemistry and biology as a member of the family of amino acids which, when combined, form the building blocks of proteins. (2) It is a relatively small molecule (~5.2 angstroms from the thiol to the hydroxyl groups) which limits the number of vibrational modes to consider when analyzing the Raman spectra and limits the effect of the variations in the geometric structure of the molecular backbone on the conductance. (3) It possesses 3 terminal functional groups that are commonly used as anchors in molecular devices, namely, a thiol, an amine, and a carboxylic acid. This allows for a variety of potential binding configurations that can occur.

To investigate the different binding configurations in cysteine, blinking measurements were performed in the same manner discussed in previous chapters. A SAM of L-cysteine (Sigma) was formed by incubating a gold substrate in a ~1 mM solution of cysteine dissolved in deionized (DI) water for ~18 hours. All substrates were flame annealed using a butane torch for ~15 seconds prior to incubation to remove any surface contamination. After incubation, the substrates were removed from the solution, rinsed with DI water, and dried gently using nitrogen gas.

To cover a wider range of potential conductance values for cysteine, two sets of experiments were performed at different biases and using amplifiers with different gains. The first set of blinking experiments were performed at an applied bias of 200mV using a 10 nA/V

transimpedance amplifier while the second set of measurements were taken using an applied bias of 100 mV using a 100 nA/V transimpedance amplifier. By doing this, it was possible to collect a larger number of samples for statistical analysis and investigate a wider range of conductance values for cysteine. All spectral data was acquired using an integration time of ~22ms and incident laser power of ~5mW. A depiction of L-cysteine in a single molecule junction can be seen in figure 6-1 below along with a sample blinking trace and Raman spectra.

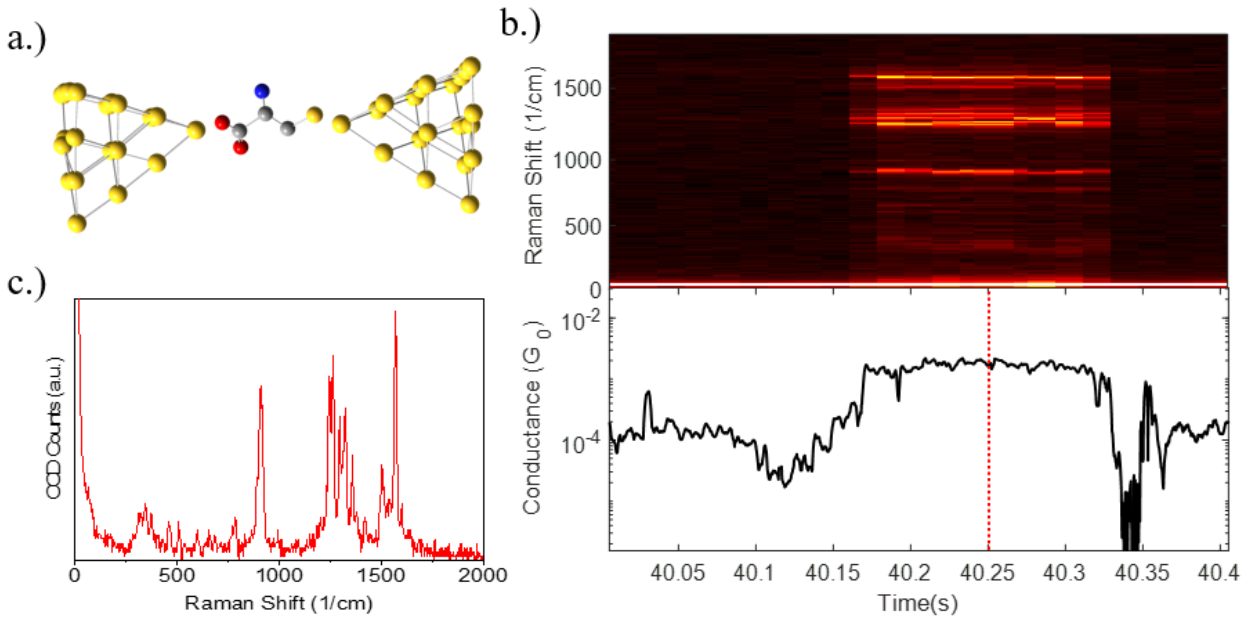

Fig. 6-1. (a) Model of a L-Cysteine single molecule junction. (b) Example of correlated Raman activity (top panel) and conductance (bottom panel) suggesting the formation of a single-molecule junction. (c) Raman spectrum associated with the time marked by the red line in the bottom panel of (b).

In this time series trace, the formation of a single-molecule junction is suggested by the abrupt increase in current at ~40.17 seconds and subsequent drop in current at ~40.34 seconds (figure 6-1b, bottom panel). The single-molecule nature is further supported by the dramatic increase in Raman scattering (figure 6-1b, top panel) at the junction that is correlated with the step-like feature in the conductance.

6.3 Results and Discussion

Given that cysteine possesses three functional group capable of binding to the gold contacts in the junction, it is expected that there are numerous configurations that can form. As such, a statistical analysis of blinking events is necessary to identify and understand the behavior of cysteine in the junction. This was done by manually identifying ~200 individual blinking events consisting of several sets of Raman spectra, resulting in a total of 1,604 Raman spectra. Post processing of the Raman spectral data was done by performing a baseline subtraction using asymptotic least squares fit. The signal-to-noise ratio (SNR) of each spectrum was then taken using a Raman spectrum with no visible peaks as the noise reference. Any Raman spectra with a SNR less than 0.5 were subsequently removed from the data set. The remaining spectra were filtered using a Savitsky-Golay filter and normalized by subtracting the minimum value of the spectrum from each pixel value and dividing it by the range of intensity values. Finally, outliers were removed from the cumulative data set by performing principal component analysis and removing any data sets that were 2.58 times the standard deviation plus/minus the mean along principal components one and two. This treatment reduced the number of spectral data sets from 1,604 to 820.

From the remaining data sets, it was then possible to create a histogram of the conductance using the average conductance associated measured at the same time as each Raman spectra. The resultant histogram of conductance given in log scale and normalized to the quantum of conductance can be seen in figure 6-2.

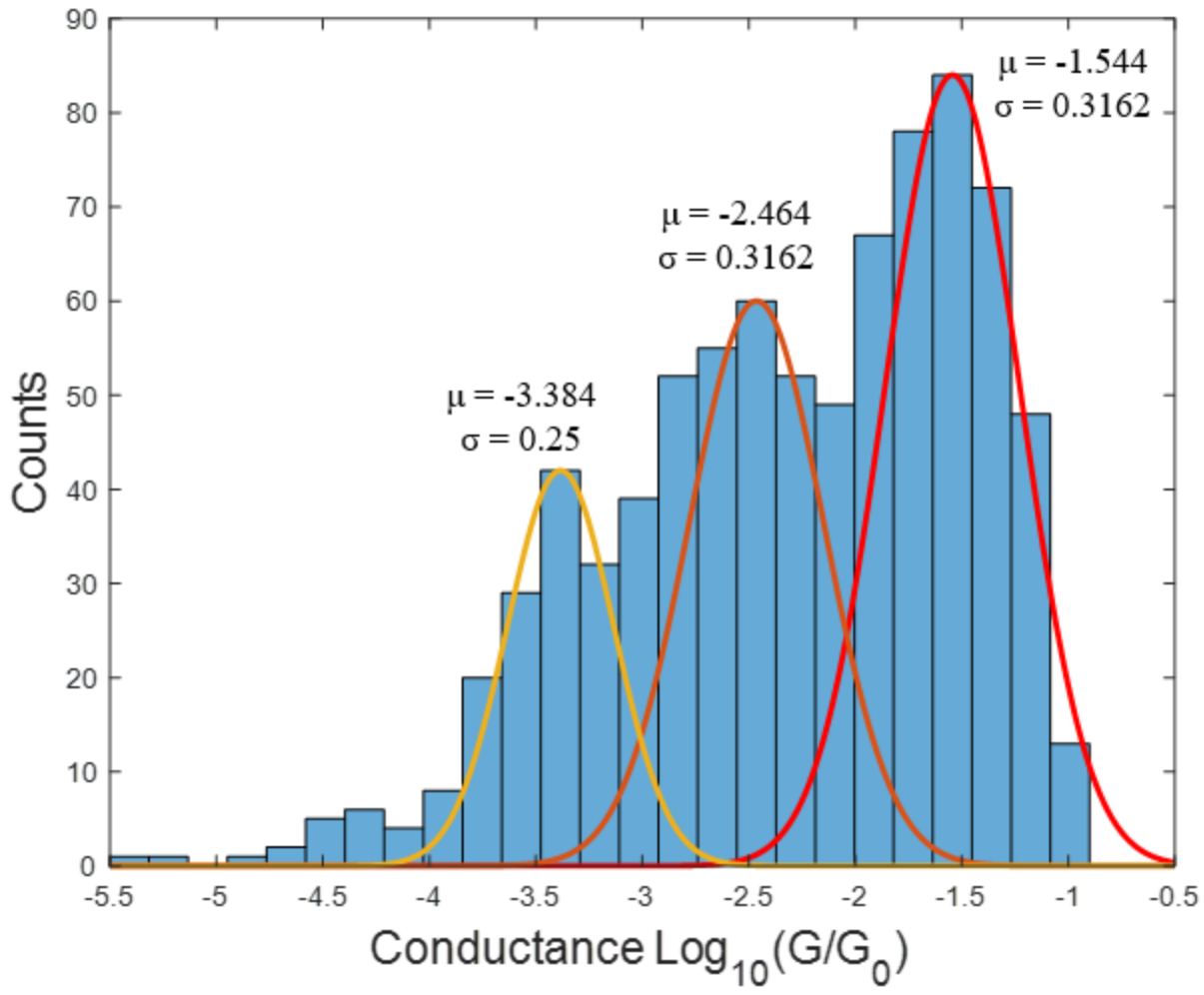

Fig. 6-2. Conductance histogram from combined cysteine blinking experiments highlighting three distinct conductance regions and the average conductance associated with each distribution.

This histogram forms a multi-modal distribution of conductance values. By fitting each mode to a gaussian distribution, we can identify three characteristic conductance values given as the mean of the distribution. In this case, a high conductance state, G_H, at -1.544 (2.86E-2 G_0), a medium conductance state, G_M, at -2.464 (3.4E-3 G_0), and a low conductance state, G_L, at -3.384 (4.13E-4 G_0).

6.3.1 Feature Importance of Spectral Data for Classifying Conductance

After identifying three unique conductance distributions for cysteine, we explored the spectral data associated with each distribution to gain insight on how the structure of the molecule influences these conductance values. However, the spectral behavior of individual peak position and intensity varies significantly over the course of a single blinking event making it challenging to consistently associate spectral features with a given mode.

To solve this problem, we trained a machine learning model to classify the spectral data using each conductance distribution as a label. It was then possible to determine a set of importance scores for each class in the model which provided insight into what spectral features were significant for assigning a conductance state to each spectrum.

The model was constructed as an ensemble of random forest binary classifiers in which each classifier was responsible for determining if a given Raman spectrum was a member of the conductance distribution. Hyper parameter tuning was performed, and the model was trained using the entire set of experimental Raman data. To mitigate the effects of overfitting 10-fold cross validation was performed. Once the classifier was trained, it was possible to calculate an importance score for each feature the classifier is acting on. This done by removing features from nodes in the random forest and observing how the classification error changes. The average error is then compared against the initial accuracy of the model when all features are included. This allows us to determine the relative importance across all features in the set. Figure 6-3 below shows the confusion matrices and importance plots for all 3 classifiers in the model.

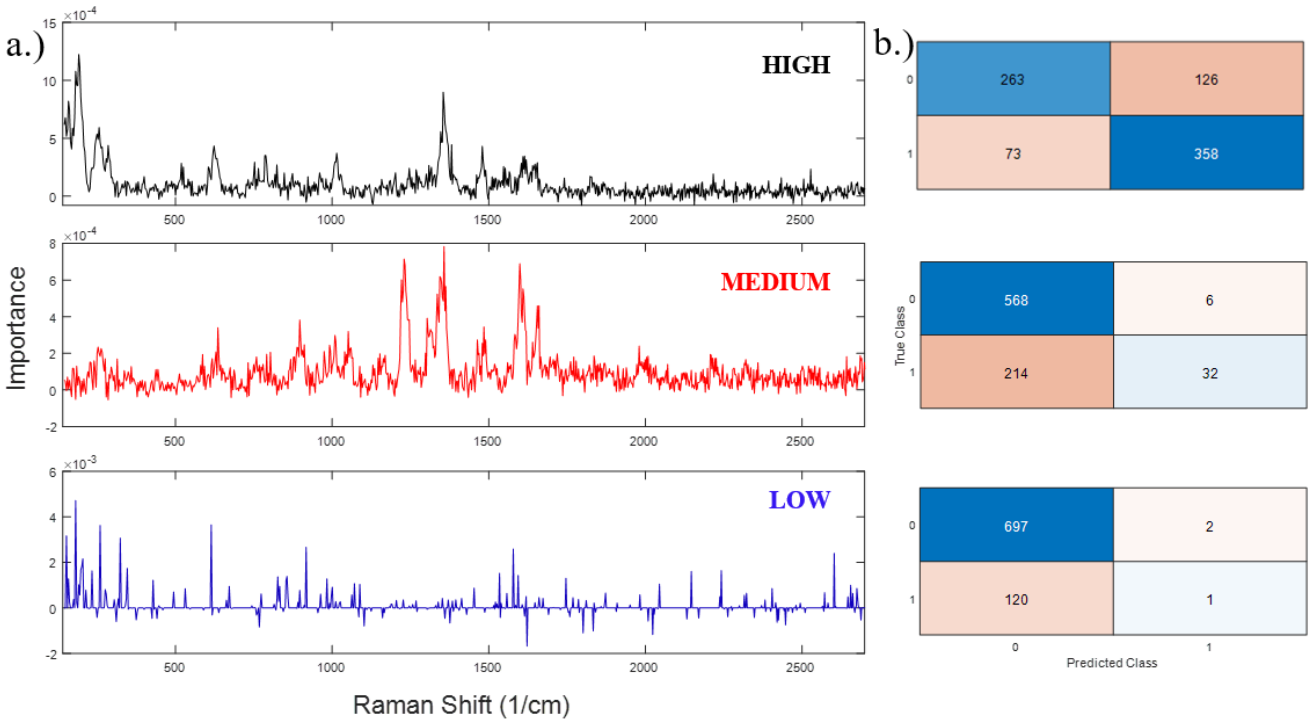

Fig. 6-3. (a) Importance plots for the high (black), medium (red), and low (blue) conductance states and (b) corresponding confusion matrices for each binary classifier.

From the plots in figure 6-3, it can be seen that each classifier is successful at identifying cases where a spectrum does not belong to a particular conductance distribution. The classifier for the high conductance is successful at identifying spectrum that belong to its distribution while the low conductance state classifier performs very poorly. The poor performance of the low conductance state classifier is further evidenced in the feature importance. Multiple gaps can be seen with either zero or negative importance values suggesting that much of the information content in these regions was not useful for the purpose of classification. This suggests that variation of spectral features in the low conductance region was much higher, possibly due to multiple configurations with similar conductance values in this region or the bound molecule has greater conformational freedom resulting in a higher variation of spectral features spectral features.

Given the poor performance of the classifier for the low conductance state, we limit our analysis to the medium and high conductance states. Analysis of the importance features show several overlapping peaks between these two plots, primarily in the fingerprint region where both classifiers place higher importance values on the peaks at 1357, 1484, 1609, and 1660 cm^{-1}. In the low wavenumber region, we additionally see in overlap in the peak at 256 cm^{-1}. In contrast, the importance plot for the medium conductance state weights the peak at 1230 cm^{-1} much more heavily than the high conductance state classifier whereas the high conductance state classifier weights several peaks in the low wavenumber region more, specifically, peaks located at 158, 191, and 285 cm^{-1}. The low wavenumber region of a Raman spectrum is typically associated with vibrational modes from heavier atoms which, for the case of a molecular junction, are related to the gold atoms and the atoms bound to them. Thus, given the greater importance placed on the low wavenumber peaks for the high conductance state, we may infer that more anchor groups are involved in the formation to the junction. This is unsurprising, as stronger coupling should increase the conductivity of the molecular junction. While at this stage, we can not provide a definitive modal analysis of the measured Raman spectrum, this analysis has suggested several distinct features to focus on for understanding the configurations of cysteine molecular junctions and their influence on conductivity.

6.3.2 Theoretical Modeling of Binding Configurations

To assist with our identification of the vibrational discussed in the previous section, we utilize DFT calculations to model several cysteine molecular junctions and establish multiple reference Raman spectra for comparison. In these simulations, the cysteine molecular junction is

modeled using two 20 atom tetrahedral gold clusters to act as the contact electrodes. Additionally, hydrogen atoms on the cysteine molecule are removed from the thiol and hydroxyl groups.

First, the geometry of the gold clusters and the free cysteine molecule are relaxed independently. Two 20 atom clusters are then positioned at a distance equal to the length of the relaxed cysteine molecule away from one another. The cysteine molecule is then placed in gap with an initial guess geometry as a possible binding configuration. To simplify these calculations, the atomic coordinates of the back layer of each gold cluster is frozen during the optimization step. Prior to calculating the Raman activity, the complete cysteine molecular junction geometry is optimized until a set of convergence criteria is met. Once a converged geometry is established, a frequency calculation is performed to determine the normal modes of vibration and their corresponding Raman activity. All calculations were performed using the Gaussian09 software package[62] using the 6-31g(d,p) basis set for the organic atoms and LANL2DZ basis set with effective core potential for the gold atoms along with the PBE1/PBE1 density functional. Figure 6-4 shows four predicted potential binding configurations for the cysteine molecule junction along with each configurations Raman spectrum.

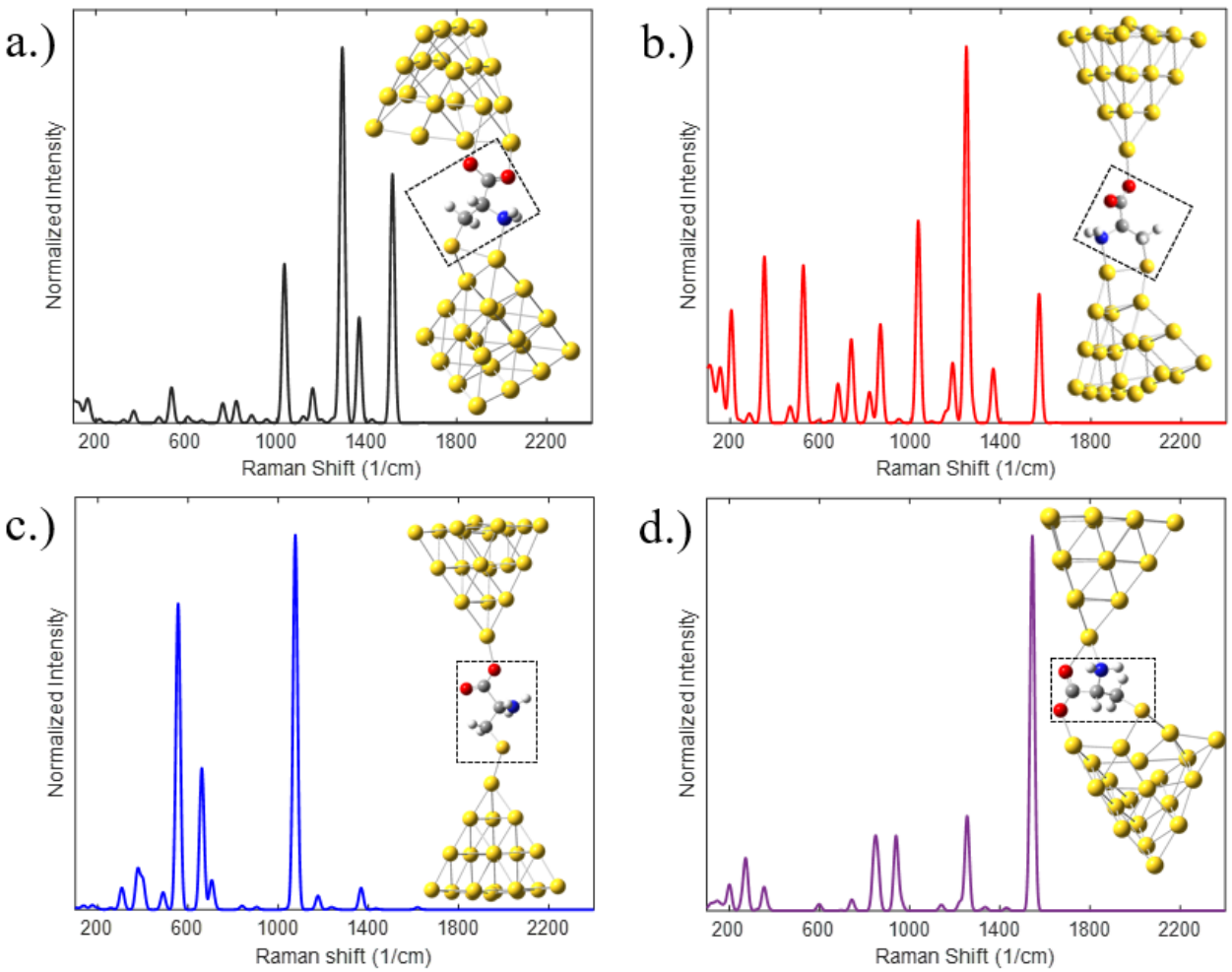

Fig. 6-4. Theoretically calculated Raman spectra for several sample cysteine binding configurations. The cysteine molecular device for each configuration is outlined in a black box in order to distinguish between sulfur and gold atoms. In the diagrams, oxygen atoms are colored red, nitrogen atoms are blue, and sulfur atoms are yellow.

In figure 6-4, the predicted binding configurations show varying degrees of complexity. Arguably the simplest configuration can be seen in figure 6-4c where the sulfur is the only atom bound to the bottom electrode and the single bonded oxygen atom (C-O) is the only atom bound to the top electrode. In figures 6-4 a and b, we can see both the sulfur and the nitrogen atoms bound to the bottom electrodes with the sulfur bound at a bridge adsorption site. Furthermore, figure 6-4a predicts a configuration in which both oxygen atoms of the carboxylic acid are bound to the top electrode, where figure 6-4b only predicts the single bonded oxygen as bound at an atop adsorption

site. Figure 6-4d depicts one of the more complicated geometries but with a spectrum that's easier to interpret. In this geometry, the oxygen atoms of the carboxylic acid are each bound to opposite gold atoms with the sulfur and nitrogen at opposite electrodes as well.

Analysis of the vibrational modes from this configuration show the most prominent modes are associated with the stretches along the backbone of cysteine namely C=O stretch (1606 cm^{-1}), C-O stretch (1305 cm^{-1}), C-C stretch (977 cm^{-1}), C-N stretch (877 cm^{-1}), and S-Au stretch (284 cm^{-1}). A comparison with figure 6-1c shows three sets of peaks in the fingerprint region with the highest wavenumber group corresponding to the most intense peak as well as a single set of peaks in the low wavenumber region suggesting that these peaks may be assigned to the backbone stretching vibrations of cysteine. While lower in intensity, these vibrational modes reside at similar frequencies for each of other predicted configurations.

It is important to note that we do not believe any one of the configurations in figure 6-4 is completely representative of either conductance distribution. Rather we wish to use these simulations to deduce information on which groups are involved more often in forming a junction for each conductance distribution.

Next, we turn our attention to the vibrational mode at 1230 cm^{-1} that was heavily weighted in the medium conductance state model. Looking at figure 6-4 b and c, we can see their most intense peaks are located at 1247 and 1075 cm^{-1} respectively. In both cases, this corresponds to a bending of the carboxylic acid. Furthermore, both of these models involve only the single bonded oxygen atom (C-O) bonding to the gold cluster. This suggests, that in our medium conductance state, it is common for only one of the oxygens to bind in the junction whereas the lower importance for the high state suggests that both oxygens are involved in bond formation.

Furthermore, looking at the increased activity in the low wavenumber region of the importance plots suggest both thiol and amine bonding for junction formation in the high conductance state.

6.4 Conclusion

In conclusion, this work demonstrates the utility of JERCS for identifying binding configurations in systems that possess multiple, complex binding motifs. While it is challenging to identify every mode in single-molecule Raman measurements, we have shown that through the assistance of machine learning models, we can identify key features in the spectral data associated with different conductance states which can then be better understood with the help of theoretical simulations. This work acts shows that it is possible to directly measure characteristic features related to the binding configuration of single-molecule junctions as well as provides a unique approach for interpreting spectral data from single-molecule Raman scattering.

CHAPTER 7

Additional Applications for JERCS: Identification of Single-Amino Acids

7.1 Introduction

Thus far, the discussion of JERCS has been limited to its utility in the field of molecular electronics, however, it is also particularly attractive for applications in biology and chemistry due to its tremendous sensitivity for chemical identification. Identification of chemical species has been widely demonstrated using tunneling currents in nanogaps. In particular, recognition tunneling[68] has been gaining traction as an approach for DNA and protein sequencing. While successful, it is still challenging to distinguish between individual amino acids which may only differ in composition by a single atom. To this end, JERCS is an ideal candidate for identifying amino acids as it provides characteristic information on the structure in the form of a tunneling current as well as in-depth structural information from the Raman scattered light. One of the major drawbacks of single molecule Raman spectroscopy is the interpretation of the results which can fluctuate greatly due to molecular reorganization. Discriminating between amino acids at the single molecule level is further complicated due to their low symmetry which makes their spectral fingerprint exceptionally sensitive to configuration changes within the inhomogeneous plasmonic fields created by the optically excited junction. While powerful, utilization of single-molecule Raman scattering for sequencing purposes is still underdeveloped.

In this chapter, we perform a study on a subset of amino acids using JERCS to demonstrate the possibility of identifying single amino acids using their combined conductance and spectral fingerprints. While separating different amino acids by their spectral or conductance signature

alone is challenging, using this combined information in tandem with machine learning approaches developed in chapter 6, allows for highly reliable identification of single amino acids.

7.2 JERCS Measurements of Amino Acids

For this study, we chose to analyze the conductance and Raman response of 7 of the 21 amino acids. Figure 7-1 depicts the amino acids under scrutiny, namely: cysteine, glycine, alanine, tyrosine, leucine, asparagine, and serine. The general structure of amino acids consists of an amino group ($-NH_3^+$) and a carboxylic acid group ($-CO_2H$) as the base structure with the inclusion of a side chains whose structure dictates the species of amino acids. This choice of subset of amino acids allows us to scrutinize the simplest amino acid, glycine, and observe how the Raman spectrum and conductivity changes as the functional group of the side chain is modified. These modifications can consist of only 2 atoms in the case of alanine or scale to more complicated cyclic structures in the case of tyrosine.

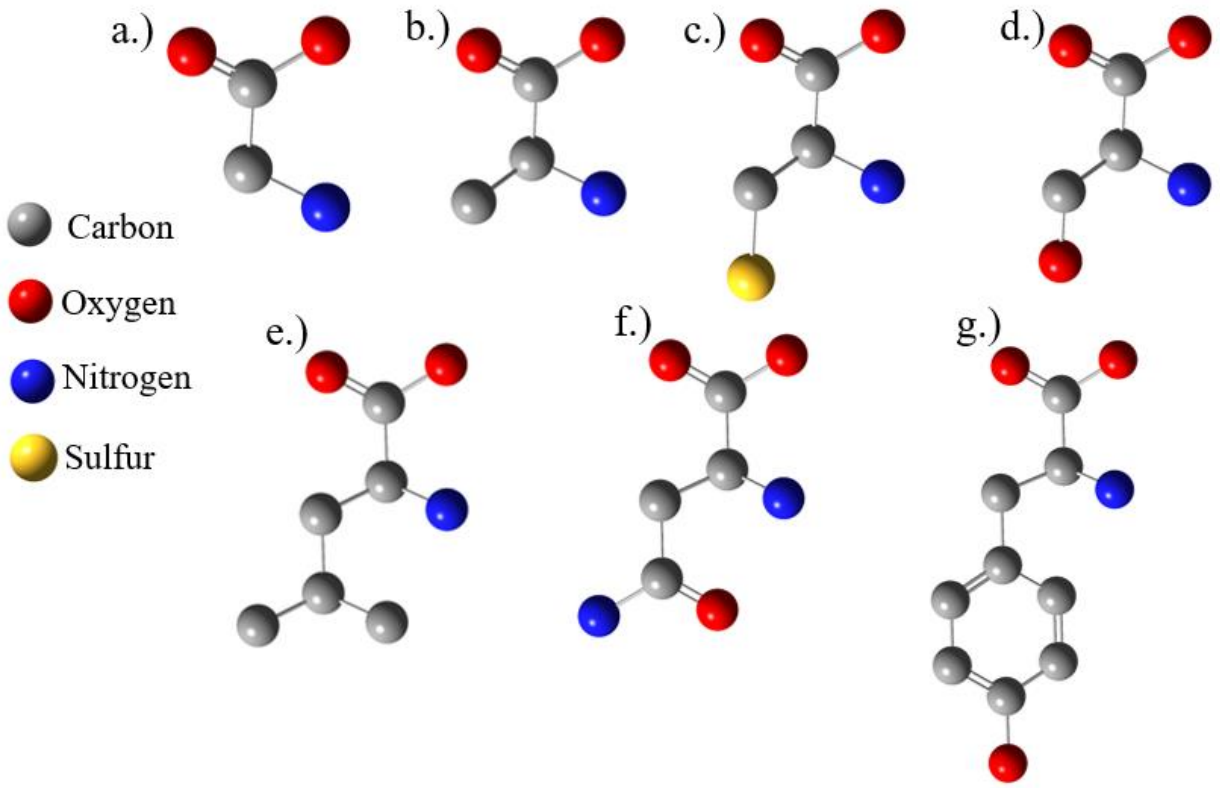

Fig. 7-1. Depictions of amino acids investigated during this study arranged by relative complexity. Hydrogen atoms have been excluded for visibility. (a) glycine, (b) alanine, (c) cysteine, (d) serine, (e) leucine, (f) asparagine, and (g) tyrosine.

In order to observe the evolution of the Raman spectral and conductive response of these amino acids, we carried out JERCS measurement in the same manner discussed in chapters 5 and 6. SAMs of each amino acid were formed on gold substrates by submerging the substrates in an ~1mM solution of a given amino acid in DI water for ~18 hours. After incubation, the surface of the substrate was rinsed with DI water and dried with a gentle nitrogen flow. All substrates were flame annealed for ~15 seconds prior to incubation. JERCS measurements were carried out at variable bias voltages ranging from 30-200 mV depending on the amino acid under investigation. Examples of blinking events for glycine, leucine, and tyrosine can be seen in figure 7-2 along with select single spectra acquired during the blinking event.

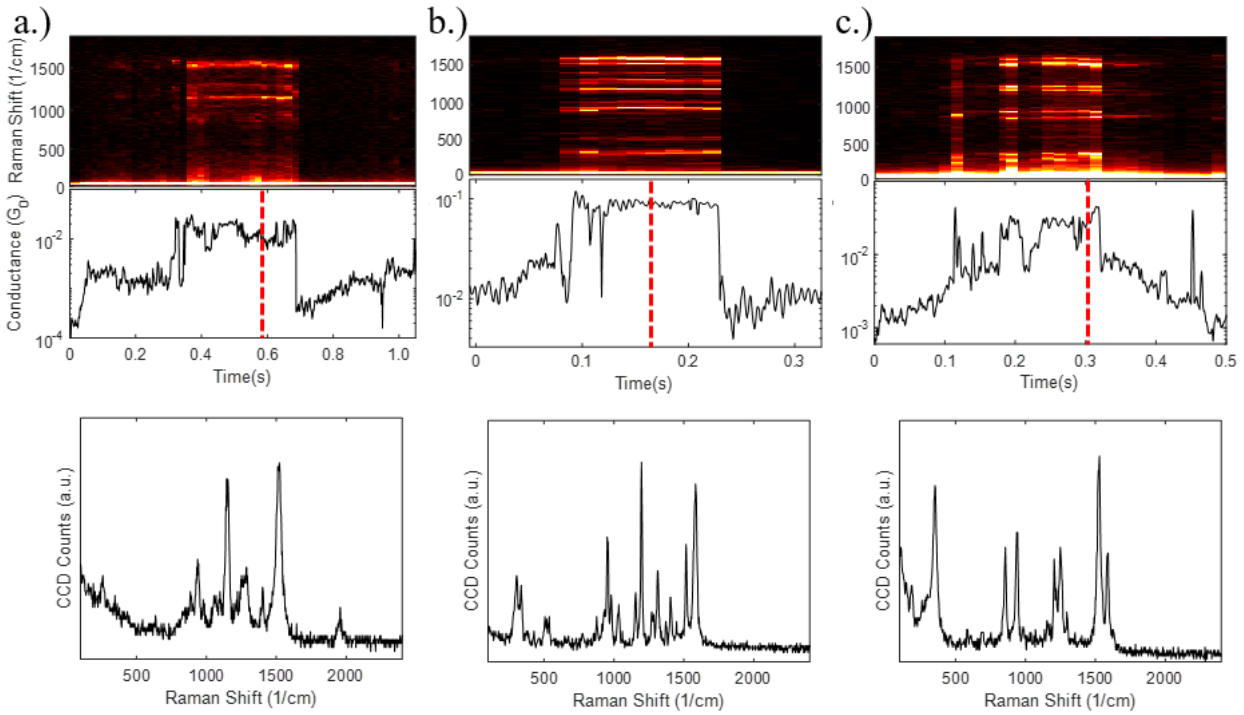

Fig. 7-2. (Top panel) Select blinking traces from JERCS measurements of (a) tyrosine, (b) leucine, and (c) glycine. (Bottom panel) Single spectra acquired from the time series in the panels above. The point the spectra was recorded is marked by the red dotted line.

As discussed in chapters 5 and 6, blinking events are characterized by plateau like features in the conductance where an abrupt increase in tunneling current is indicative of a single molecule binding between the tip and substrate followed by and steady current representing the conductance of the single molecule at a set bias and a subsequent drop in tunneling current suggesting a break in the junction. The single-molecule nature of this event is further substantiated by a drastic increase in the Raman scattering activity while the molecular junction is formed.

After performing JERCS measurements on each of the seven amino acids, blinking events were manually identified for each molecule and agglomerated into a single data set for analysis. Post processing of spectral data and removal of noisy data and outliers was done following the same procedure outlined in chapter 6. This resulted in a total of 4,498 Raman spectra and average

conductance values across all amino acids in this study. The distribution of data points for each amino acid is shown below in table 7-1.

Amino Acid	Number of Data Points in Set
Cysteine	820
Glycine	186
Alanine	401
Tyrosine	367
Leucine	747
Asparagine	1215
Serine	762

Table 7-1. Distribution of Amino Acid Data

Due to the sporadic behavior of the Raman spectrum over the duration of a blinking event, it is difficult to compare single spectra across a single molecular species let alone a family of molecules. To understand the response of each molecule, the average spectra across all data points was taken along with histograms of their recorded conductance values which can be seen in figure 7-3. While the variation of peak position and intensity of field-enhanced Raman spectra vary substantially across data points, the average spectrum for each amino acid are nearly identical. This makes identification by spectral features alone untenable. However, looking at the conductance histograms, we can see subtle differences in the different distributions between amino acids. This suggests that by combining information from the Raman spectrum and conductance data it is possible to classify individual amino acids using JERCS.

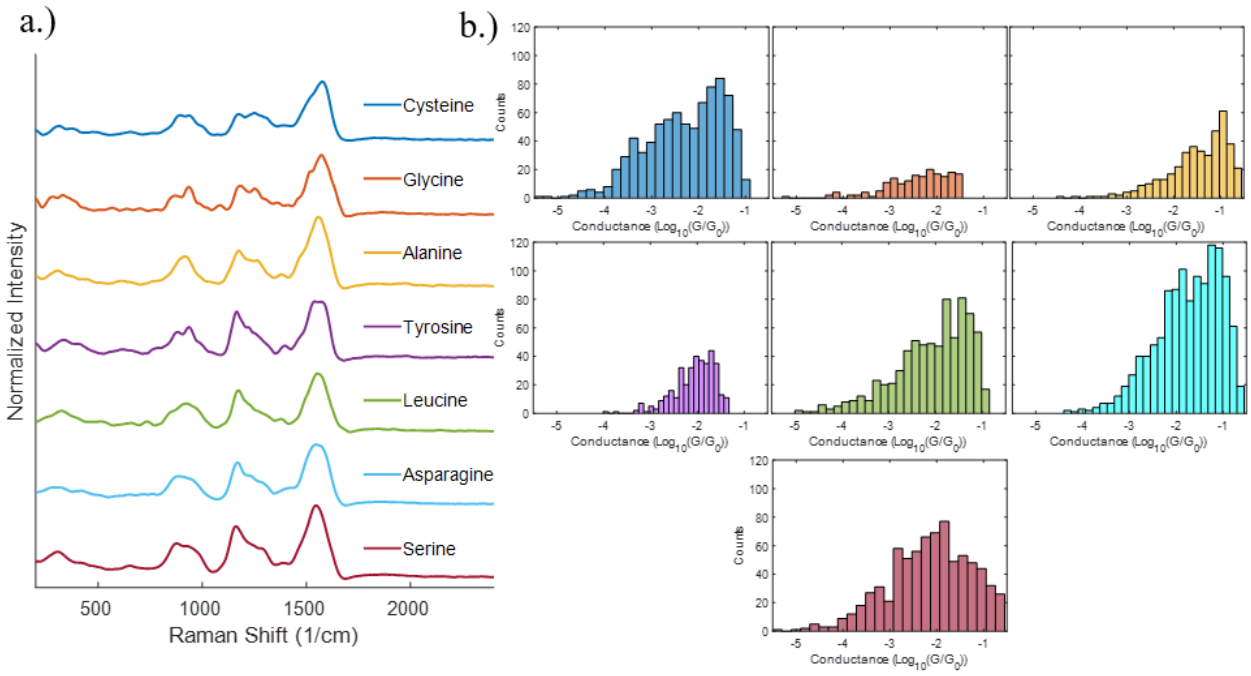

Fig. 7-3. (a) Average Raman spectra across all measurements for each amino acid and (b) corresponding conductance histograms for each amino acid.

7.3 Machine Learning Analysis of Amino Acids

To show that it is possible to identify a single-amino acid using information from its conductance and Raman spectrum, we leveraged a machine learning model similar to the one described in chapter 6. In this case, the model includes conductance information, and the class labels are taken to be amino acid each data point is associated with. Once again, we utilize an ensemble of binary classifiers in the form of random forests to decide the spectrum, conductance pair of data is a particular amino acid or not. Hyper parameter tuning was performed, and the model was trained using the entire set of amino acid samples. 10-fold cross validation was done to minimize any overfitting of the data. Confusion matrices for each binary classifier can be seen below in figure 7-4.

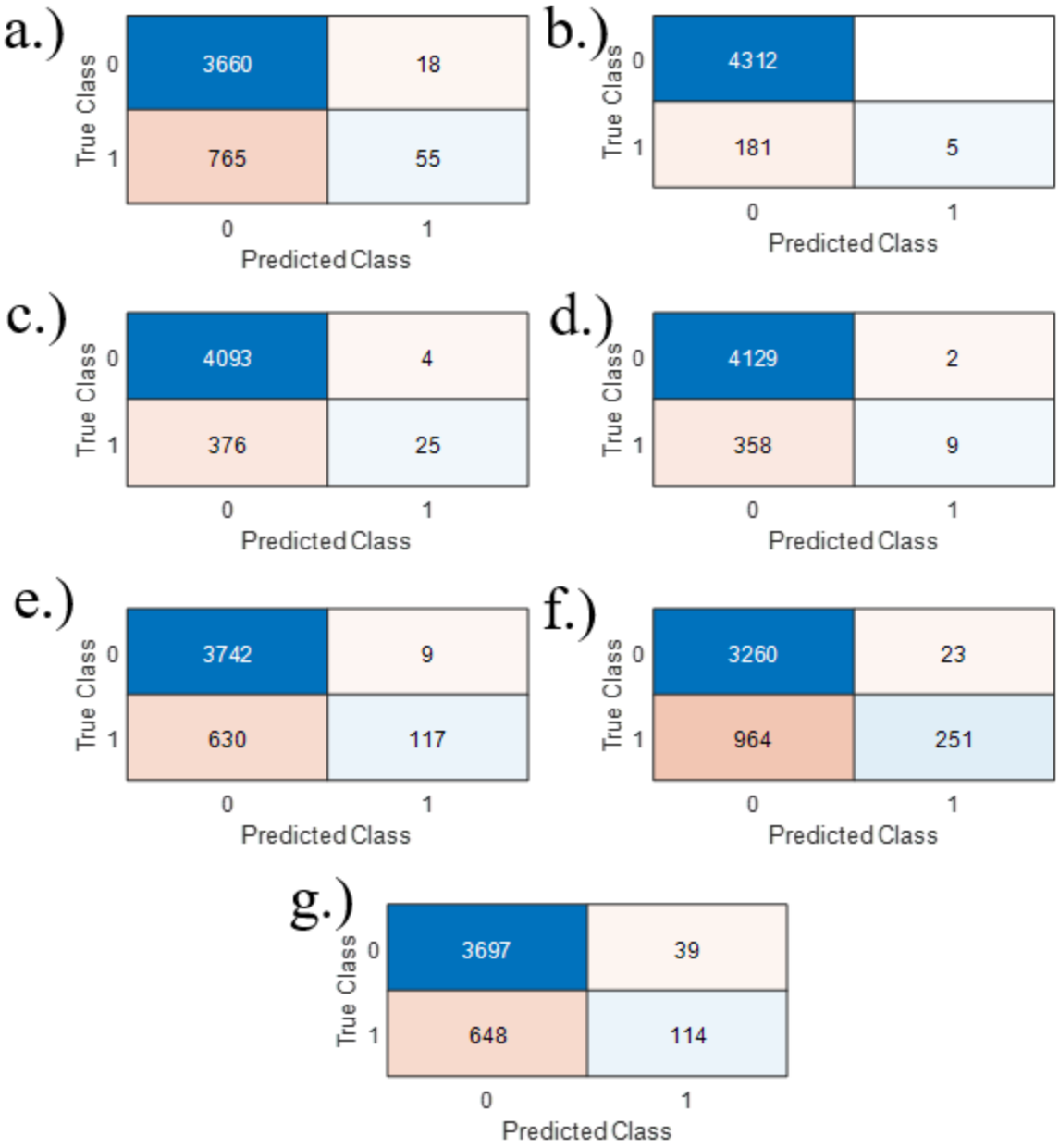

Fig. 7-4. Confusion matrices for binary classifiers for (a) cysteine, (b) glycine, (c) alanine, (d) tyrosine, (e) leucine, (f) asparagine, and (g) serine.

Analysis of these confusion matrices shows that the model employed here is highly successful at identifying when a Raman, conductance pair of data does not belong to a given amino acid but fails often fails to identify data that does belong to its correct class label resulting in a high number of false positives. Cases where the false positive rate is increasingly high in comparison

to the true positive rate suggest a higher degree of variability among the feature set, however it is expected that more balanced data sizes will reduce the number of false positives occurring. The balanced accuracy of each classifier is summarized in table 7-2.

Amino Acid	Balanced Accuracy
Cysteine	83%
Glycine	96%
Alanine	92%
Tyrosine	92%
Leucine	86%
Asparagine	78%
Serine	85%

Table 7-2. Balanced accuracy of binary classifiers for each amino acid

Using this model, we once again calculated the importance score of each feature in the data set for each binary classifier. Importance plots across all features in the data set can be seen in figure 7-5. From this these plots, we can see the relative importance of spectral lines and conductance for classifying each amino. In particular we can see that conductance information was substantially more important than any spectral lines for classifying asparagine and alanine. On the other hand, the conductance of glycine and serine was negligible for classification. Of particular interest is the importance plots for cysteine and tyrosine where the conductance is equally as important as the Raman peak positions. This result demonstrates that classification of amino acids

at the single molecule level requires information from both the molecule's conductance and Raman spectrum to be successful.

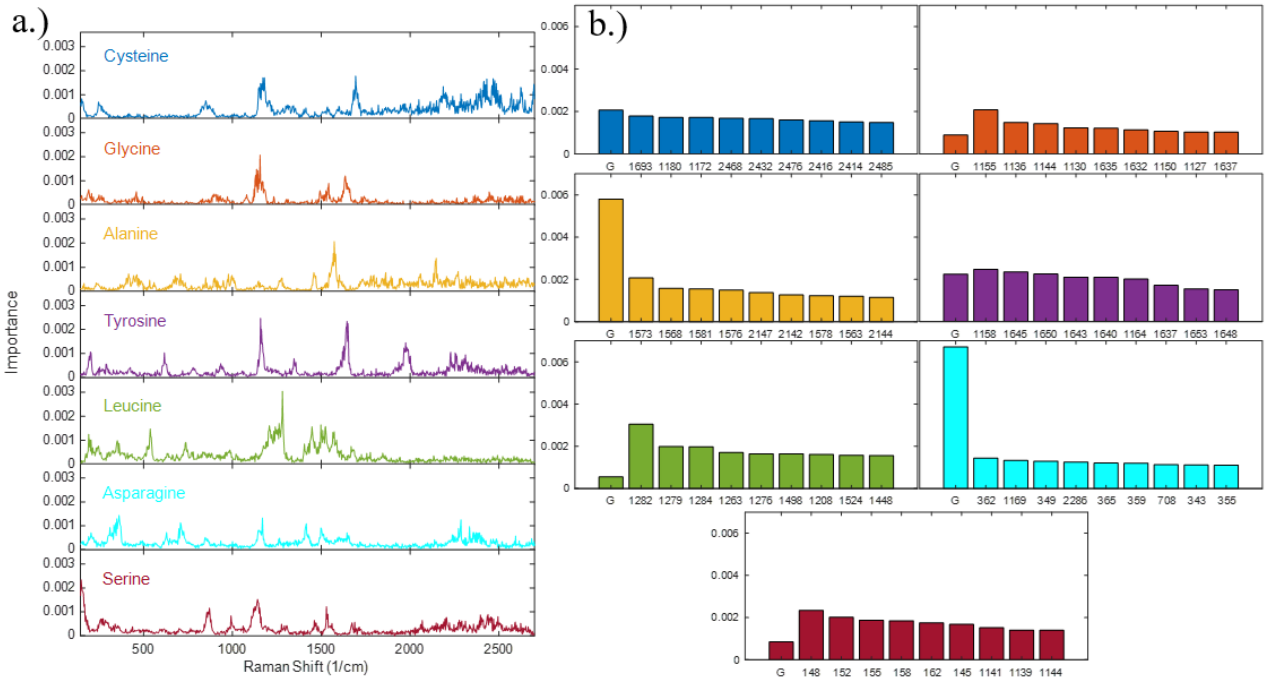

Fig. 7-5. (a) Importance plots for each amino acid and (b) importance of conductance compared to the importance of 9 most important features for the purpose of classification.

7.4 Conclusion

In conclusion, this work demonstrates several key results. First, it is possible to reliably measure the conductance and Raman spectrum of multiple amino acids. Next, we have demonstrated that the amino acids investigated in this study can be successfully classified using this information alone. Finally, we have shown that in certain cases, either the conductance or the single-molecule Raman spectrum may be used independently for classification but in order to successfully identify all amino acids it is necessary to have both pieces of information. Together, these results show both the power and need for JERCS for single-molecule chemical analysis. While this work focused on a subset of amino acids, it is clear that it can easily be extended to the

complete set as well as nucleic acids presenting the possibility of sequencing single peptides, proteins, and even strands of DNA or RNA. Furthermore, the impressive sensitivity to configuration and environment extends the potential of this method beyond classification and will allow for the investigation of structural changes in complex biochemical systems and how such changes influence chemical reactions, catalysis, tautomerization, and so on.

CHAPTER 8

Summary and Future Work

8.1 Summary

This dissertation demonstrated a novel platform for simultaneously measuring the conductance and Raman response of a chemical system with single-molecule resolution. The apparatus was designed as a laterally configured STM-BJ system that could be used independently and cooperatively with a commercially purchased confocal Raman microscope system allowing the user to measure the electrical and Raman scattering response of single-molecule systems. The ultra-sharp tips used in STM systems acts as a means of contacting single molecules for electrical measurements and also acts as a so-called "lightning rod" when excited by a laser, creating an extremely intense and localized electric field around the molecule. This allows for mutually verifiable evidence of single-molecule sensitivity as well as a means of interrogating the molecule electrically, mechanically, and optically to view dynamic structural changes resulting from these perturbations. The function of this system was demonstrated by measuring the electrical and optical response on a SAM of BPDT and comparing it with previously reported results. Upon successful demonstration of a working system, it was possible to probe key features in single-molecule systems that directly impact their conductivity and show the utility of such measurements beyond the field of molecular electronics.

First, we performed a deeper investigation on the dynamics of BPDT systems to observe how structural changes of this molecule directly influence the ability of the molecule to conduct electricity. While the interpretation of Raman spectra is complicated, by utilizing machine learning algorithms, in this case k-means clustering, we were able to identify shifts in peak frequencies

suggesting mechanical deformation of the molecule due to the unstable junction. This allowed us to identify individual blinking events where we could track the evolution of a peaks position and conductance over time. Using, DFT it was possible to theoretically calculate the evolution of the Raman peak position as a function of applied strain and identify structures whose configurations are representative of what was seen in the experimental data. The conductance of these structures was then determined using the energy levels determined through DFT calculations as an input to the NEGF method for calculating transmission. By using the coupling of the junction to the electrodes as a tuning parameter, it was possible to establish the zero-bias conductance of each junction allowing us to paint a picture of the dynamics it experiences under mechanically induced strain.

Next, we wished to investigate the affect anchoring groups had on the conductance of single-molecule junctions. To this end we chose to investigate the configuration and conductance variation of cysteine, an amino acid possessing three functional groups capable of binding to the gold contacts of our single molecule junction: a thiol, an amine, and a carboxylic acid. JERCS measurements were performed on cysteine molecular junctions to cultivate a data set large enough for a statistical analysis. Conductance histograms of the cumulative data showed three distinct distributions in the conductance. By training a machine learning model to classify a given Raman spectra with each conductance it is associated with, it was possible to identify key features that were important for this process. Comparing these features with theoretical Raman spectra predicted from DFT models, we could then identify specific junction configurations with each distribution in the conductance histogram.

Lastly, we demonstrated the utility of this technique to fields outside molecular electronics, specifically chemical analysis, and identification. To do this, we performed JERCS measurements

on a subset of amino acids. A data set of Raman spectra and conductance values was built for each amino acid and used to train a series of binary classifiers to assign data points to their appropriate amino acid label using the combined Raman scattering and conductance information. Analysis of the confusion matrices showed excellent performance for identifying instances when a spectrum was not a member of a given amino acid class but also displayed a high false positive rate. It is expected that the inclusion of more data sets in the model would improve this rate. However, investigation of the importance score of data set features showed that the relative importance of conductance and Raman scattering varied between amino acids, thus highlighting the need for both pieces of information if one is interested in classifying the whole series and emphasizing the need for JERCS to tackle this endeavor.

8.2 Future Work

8.2.1 Identifying the Structural Influence on Tunneling and Hopping Transport Systems

In chapter 2 of this dissertation, we discussed the need to directly interrogate the structural information of a single-molecule junction to provide deeper insight into the transport mechanisms of families of molecules and how these mechanisms change as the molecules become longer or as a function of temperature. Particularly in the case of hopping transport, charge occupies the molecular energy levels and induces a reorganization of the molecule's internal structure. By observing distinct changes in the molecular structure during transport, it is possible to verify hopping transport and better understand how these configuration changes impact the molecule's conductivity.

8.2.2 Exploring Charge Induced Conformational Changes in Proteins

At the end of chapter 7, we emphasized the potential for not only identifying biological macromolecules but also the possibility of probing their structural dynamics as well. This work would demonstrate this possibility by observing conformational changes in proteins containing redox active metallic centers like the blue copper protein, azurin. In this molecule, the protein exhibits different configurations based on the oxidation state of the copper atom it contains. By manipulating this state and identifying changes in the Raman scattering, it would be possible to demonstrate the ability of JERCS to understand configurations of single-molecule systems as small as amino acids and as large as proteins opening the door for the next generation of chemical analysis.

8.2.3 Observing Local Currents and QI Effects with AS Raman Scattering

One of the remarkable phenomena that occurs in molecular scale devices is that of quantum interference which results in sharp resonances and anti-resonances in the charge transmission due to the wavelike nature of transporting electrons. It has been theorized that IETS may be used to observe scattering from inelastic tunneling through molecular junctions of 1,3-benzendithiol due to interfering pathways[69], however, this has yet to be demonstrated. It was discussed previously in chapters 3 and 4 that anti-Stokes Raman scattering may also be used as a means of measuring electron-phonon interactions due to inelastic scattering thus by observing and quantifying the interaction of current flow with specific modes in junctions of 1,3-benzenedithiol it is possible to identify local current pathways at the single-molecule level from the Raman scattering.

REFERENCES

[1] A. Aviram and M. A. Ratner, “Molecular Rectifiers,” *Chem. Phys. Lett.*, vol. 29, no. 2, pp. 277–283, Nov. 1974.

[2] B. Capozzi *et al.*, “Single-molecule diodes with high rectification ratios through environmental control,” *Nat. Nanotechnol.*, vol. 10, no. 6, pp. 522–527, Jun. 2015, doi: 10.1038/nnano.2015.97.

[3] M. L. Perrin, E. Burzuri, and H. S. J. Van Der Zant, “Single-molecule transistors,” *Chem. Soc. Rev.*, vol. 44, no. 4, pp. 902–919, 2015.

[4] H. B. Li, B. E. Tebikachew, C. Wiberg, K. Moth-Poulsen, and J. Hihath, “A Memristive Element Based on an Electrically Controlled Single-Molecule Reaction,” *Angew. Chem. - Int. Ed.*, pp. 2–8, 2020, doi: 10.1002/anie.202002300.

[5] T. Ghomian, O. Kizilkaya, L. K. Domulevicz, and J. Hihath, “Molecular quantum interference effects on thermopower in hybrid 2-dimensional monolayers,” *Nanoscale*, vol. 14, no. 16, pp. 6248–6257, 2022, doi: 10.1039/D2NR01731H.

[6] L. Bogani and W. Wernsdorfer, “Molecular spintronics using single-molecule magnets,” *Nat. Mater.*, vol. 7, no. 3, pp. 179–186, Mar. 2008, doi: 10.1038/nmat2133.

[7] A. B. Zrimsek *et al.*, “Single-Molecule Chemistry with Surface- and Tip-Enhanced Raman Spectroscopy,” *Chem. Rev.*, vol. 117, no. 11, pp. 7583–7613, 2017, doi: 10.1021/acs.chemrev.6b00552.

[8] B. Xu and N. J. Tao, “Measurement of single-molecule resistance by repeated formation of molecular junctions,” *Science*, 2003, doi: 10.1126/science.1087481.

[9] P. Gehring, J. M. Thijssen, and H. S. J. van der Zant, “Single-molecule quantum-transport phenomena in break junctions,” *Nat. Rev. Phys.*, vol. 1, no. 6, pp. 381–396, Jun. 2019, doi: 10.1038/s42254-019-0055-1.

[10] J. H. Tian *et al.*, “Study of molecular junctions with a combined surface-enhanced raman and mechanically controllable break junction method,” *J. Am. Chem. Soc.*, vol. 128, no. 46, pp. 14748–14749, 2006, doi: 10.1021/ja0648615.

[11] D. Natelson *et al.*, “Simultaneous Measurements of Electronic Conduction and Raman Response in Molecular Junctions,” *Nano Lett.*, vol. 8, no. 3, pp. 919–924, 2008, doi: 10.1021/nl073346h.

[12] Z. Liu *et al.*, “Revealing the molecular structure of single-molecule junctions in different conductance states by fishing-mode tip-enhanced Raman spectroscopy,” *Nat. Commun.*, vol. 2, no. 1, 2011, doi: 10.1038/ncomms1310.

[13] J. C. Cuevas and E. Scheer, *Molecular Electronics: An Introduction to Theory and Experiment*. World Scientific, 2017.

[14] S. Datta, *Quantum Transport: Atom to Transistor*. Cambridge University Press, 2005.

[15] X.-Y. Zhou, Z.-L. Peng, Y.-Y. Sun, L.-N. Wang, Z.-J. Niu, and X.-S. Zhou, “Conductance measurement of pyridyl-based single molecule junctions with Cu and Au contacts,” *Nanotechnology*, vol. 24, no. 46, p. 465204, Nov. 2013, doi: 10.1088/0957-4484/24/46/465204.

[16] S. Kaneko, T. Nakazumi, and M. Kiguchi, “Fabrication of a Well-Defined Single Benzene Molecule Junction Using Ag Electrodes,” *J. Phys. Chem. Lett.*, vol. 1, no. 24, pp. 3520–3523, Dec. 2010, doi: 10.1021/jz101506u.

[17] C. Jia *et al.*, “Covalently bonded single-molecule junctions with stable and reversible photoswitched conductivity,” *Science*, vol. 352, no. 6292, pp. 1443–1445, Jun. 2016, doi: 10.1126/science.aaf6298.

[18] A. C. Aragonès, N. Darwish, S. Ciampi, F. Sanz, J. J. Gooding, and I. Díez-Pérez, “Single-molecule electrical contacts on silicon electrodes under ambient conditions,” *Nat. Commun.*, vol. 8, no. 1, p. 15056, Apr. 2017, doi: 10.1038/ncomms15056.

[19] S. Schmaus *et al.*, “Giant magnetoresistance through a single molecule,” *Nat. Nanotechnol.*, vol. 6, no. 3, pp. 185–189, Mar. 2011, doi: 10.1038/nnano.2011.11.

[20] R. Yamada, M. Noguchi, and H. Tada, “Magnetoresistance of single molecular junctions measured by a mechanically controllable break junction method,” *Appl. Phys. Lett.*, vol. 98, no. 5, p. 053110, Jan. 2011, doi: 10.1063/1.3549190.

[21] F. Chen, X. Li, J. Hihath, Z. Huang, and N. Tao, “Effect of Anchoring Groups on Single-Molecule Conductance: Comparative Study of Thiol-, Amine-, and Carboxylic-Acid-Terminated Molecules,” *J. Am. Chem. Soc.*, vol. 128, no. 49, pp. 15874–15881, Dec. 2006, doi: 10.1021/ja065864k.

[22] L. Venkataraman, J. E. Klare, I. W. Tam, C. Nuckolls, M. S. Hybertsen, and M. L. Steigerwald, “Single-molecule circuits with well-defined molecular conductance.,” *Nano Lett.*, vol. 6, no. 3, pp. 458–62, 2006, doi: 10.1021/nl052373+.

[23] A. Mishchenko *et al.*, “Single-molecule junctions based on nitrile-terminated biphenyls: A promising new anchoring group,” *J. Am. Chem. Soc.*, vol. 133, no. 2, pp. 184–187, 2011, doi: 10.1021/ja107340t.

[24] D. Krüger, H. Fuchs, R. Rousseau, D. Marx, and M. Parrinello, “Pulling Monatomic Gold Wires with Single Molecules: An Ab Initio Simulation,” *Phys Rev Lett*, vol. 89, no. 18, p. 186402, Oct. 2002, doi: 10.1103/PhysRevLett.89.186402.

[25] K. H. Müller, “Effect of the atomic configuration of gold electrodes on the electrical conduction of alkanedithiol molecules,” *Phys. Rev. B - Condens. Matter Mater. Phys.*, vol. 73, no. 4, pp. 1–6, 2006, doi: 10.1103/PhysRevB.73.045403.

[26] J. A. Malen, P. Doak, K. Baheti, T. D. Tilley, R. A. Segalman, and A. Majumdar, “Identifying the Length Dependence of Orbital Alignment and Contact Coupling in Molecular Heterojunctions,” *Nano Lett.*, vol. 9, no. 3, pp. 1164–1169, Mar. 2009, doi: 10.1021/nl803814f.

[27] J. He *et al.*, “Electronic Decay Constant of Carotenoid Polyenes from Single-Molecule Measurements,” *J. Am. Chem. Soc.*, vol. 127, no. 5, pp. 1384–1385, Feb. 2005, doi: 10.1021/ja043279i.

[28] A. Tan *et al.*, “Effect of Length and Contact Chemistry on the Electronic Structure and Thermoelectric Properties of Molecular Junctions,” *J. Am. Chem. Soc.*, vol. 133, no. 23, pp. 8838–8841, Jun. 2011, doi: 10.1021/ja202178k.

[29] L. Venkataraman, J. E. Klare, C. Nuckolls, M. S. Hybertsen, and M. L. Steigerwald, "Dependence of single-molecule junction conductance on molecular conformation," *Nature*, vol. 442, no. 7105, pp. 904–907, Aug. 2006, doi: 10.1038/nature05037.

[30] J. M. van Ruitenbeek *et al.*, "Adjustable nanofabricated atomic size contacts," *Rev. Sci. Instrum.*, vol. 67, no. 1, pp. 108–111, Jan. 1996, doi: 10.1063/1.1146558.

[31] Zotti *et al.*, "Can One Define the Conductance of Amino Acids?," *Biomolecules*, vol. 9, no. 10, p. 580, Oct. 2019, doi: 10.3390/biom9100580.

[32] H. Jeong, H. B. Li, L. Domulevicz, and J. Hihath, "An On-Chip Break Junction System for Combined Single-Molecule Conductance and Raman Spectroscopies," *Adv. Funct. Mater.*, vol. 30, no. 28, pp. 1–10, 2020, doi: 10.1002/adfm.202000615.

[33] J. C. Love, L. A. Estroff, J. K. Kriebel, R. G. Nuzzo, and G. M. Whitesides, "Self-Assembled Monolayers of Thiolates on Metals as a Form of Nanotechnology," *Chem. Rev.*, vol. 105, no. 4, pp. 1103–1170, Apr. 2005, doi: 10.1021/cr0300789.

[34] W. Haiss, R. J. Nichols, H. Van Zalinge, S. J. Higgins, D. Bethell, and D. J. Schiffrin, "Measurement of single molecule conductivity using the spontaneous formation of molecular wires," *Phys. Chem. Chem. Phys.*, 2004, doi: 10.1039/b404929b.

[35] N. Xin *et al.*, "Concepts in the design and engineering of single-molecule electronic devices," *Nat. Rev. Phys.*, vol. 1, no. 3, pp. 211–230, Mar. 2019, doi: 10.1038/s42254-019-0022-x.

[36] L. Domulevicz, H. Jeong, N. K. Paul, J. S. Gomez-Diaz, and J. Hihath, "Multidimensional Characterization of Single-Molecule Dynamics in a Plasmonic Nanocavity," *Angew. Chem. Int. Ed.*, p. anie.202100886, Apr. 2021, doi: 10.1002/anie.202100886.

[37] T. Hines *et al.*, "Transition from Tunneling to Hopping in Single Molecular Junctions by Measuring Length and Temperature Dependence," *J. Am. Chem. Soc.*, vol. 132, no. 33, pp. 11658–11664, Aug. 2010, doi: 10.1021/ja1040946.

[38] H. B. Li *et al.*, "Temperature-Dependent Tunneling in Furan Oligomer Single-Molecule Junctions," *ACS Sens.*, p. acssensors.0c02278, Feb. 2021, doi: 10.1021/acssensors.0c02278.

[39] B. C. Stipe, M. A. Rezaei, and W. Ho, "Single-Molecule Vibrational Spectroscopy and Microscopy," *Science*, vol. 280, no. 5370, pp. 1732–1735, Jun. 1998, doi: 10.1126/science.280.5370.1732.

[40] C. V. RAMAN and K. S. KRISHNAN, "A New Type of Secondary Radiation," *Nature*, vol. 121, no. 3048, pp. 501–502, Mar. 1928, doi: 10.1038/121501c0.

[41] D. J. Griffiths and D. F. Schroeter, *Introduction to Quantum Mechanics*, 3rd ed. Cambridge University Press, 2018. doi: 10.1017/9781316995433.

[42] D. A. Long, *The Raman effect: a unified treatment of the theory of Raman scattering by molecules. 2002*, vol. 8. 2002, p. 22. doi: 10.1002/0470845767.

[43] D. Harris and M. Bertolucci, *Symmetry and Spectroscopy: An Introduction to Vibrational and Electronic Spectroscopy*. New York: Dover Publications,Inc., 1989.

[44] F. A. Cotton, *Chemical Applications of Group Theory*, 3rd edition. Wiley-Interscience, 1990.

[45] E. C. Le Ru and P. G. (Pablo G. Etchegoin, *Principles of surface-enhanced Raman spectroscopy : and related plasmonic effects*. Elsevier, 2009, p. 663. [Online]. Available: http://www.sciencedirect.com/science/book/9780444527790

[46] M. Fleischmann, P. J. Hendra, and A. J. McQuillan, "Raman spectra of pyridine adsorbed at a silver electrode," *Chem. Phys. Lett.*, vol. 26, no. 2, pp. 163–166, May 1974, doi: 10.1016/0009-2614(74)85388-1.

[47] S. Nie, "Probing Single Molecules and Single Nanoparticles by Surface-Enhanced Raman Scattering," *Science*, vol. 275, no. 5303, pp. 1102–1106, 2002, doi: 10.1126/science.275.5303.1102.

[48] K. Kneipp, Y. Wang, H. Kneipp, L. T. Perelman, and I. Itzkan, "Single molecule detection using surface-enhanced Raman scattering (SERS)," *Phys. Rev. …*, vol. 78, no. 9, pp. 1667–1670, 1997, doi: 10.1103/PhysRevLett.78.1667.

[49] E. C. Le Ru, M. Meyer, and P. G. Etchegoin, "Proof of single-molecule sensitivity in Surface Enhanced Raman Scattering (SERS) by means of a two-analyte technique," *J. Phys. Chem. B*, vol. 110, no. 4, pp. 1944–1948, 2006, doi: 10.1021/jp054732v.

[50] J. A. Dieringer, R. B. Lettan, K. A. Scheidt, and R. P. Van Duyne, "A frequency domain existence proof of single-molecule surface-enhanced Raman spectroscopy," *J. Am. Chem. Soc.*, vol. 129, no. 51, pp. 16249–16256, 2007, doi: 10.1021/ja077243c.

[51] E. C. Le Ru, E. Blackie, M. Meyer, and P. G. Etchegoint, "Surface enhanced raman scattering enhancement factors: A comprehensive study," *J. Phys. Chem. C*, vol. 111, no. 37, pp. 13794–13803, 2007, doi: 10.1021/jp0687908.

[52] A. Campion, J. E. Ivanecky, C. M. Child, and M. Foster, "On the Mechanism of Chemical Enhancement in Surface-Enhanced Raman Scattering," *J. Am. Chem. Soc.*, vol. 117, no. 47, pp. 11807–11808, Nov. 1995, doi: 10.1021/ja00152a024.

[53] P. Z. El-Khoury and W. P. Hess, "Raman scattering from 1,3-propanedithiol at a hot spot: Theory meets experiment," *Chem. Phys. Lett.*, vol. 581, pp. 57–63, 2013, doi: 10.1016/j.cplett.2013.05.066.

[54] M. S. Anderson, "Locally enhanced Raman spectroscopy with an atomic force microscope," *Appl. Phys. Lett.*, vol. 76, no. 21, pp. 3130–3132, 2000, doi: 10.1063/1.126546.

[55] B. Pettinger, G. Picardi, R. Schuster, and G. Ertl, "Surface-enhanced and STM-tip-enhanced Raman spectroscopy at metal surfaces," *Single Mol.*, vol. 3, no. 5–6, pp. 285–294, 2002, doi: 10.1002/1438-5171(200211)3:5/6<285::AID-SIMO285>3.0.CO;2-X.

[56] J. Lee, K. T. Crampton, N. Tallarida, and V. A. Apkarian, "Visualizing vibrational normal modes of a single molecule with atomically confined light," *Nature*, vol. 568, no. 7750, pp. 78–82, 2019, doi: 10.1038/s41586-019-1059-9.

[57] H. Bi *et al.*, "Voltage-Driven Conformational Switching with Distinct Raman Signature in a Single-Molecule Junction," *J. Am. Chem. Soc.*, vol. 140, no. 14, pp. 4835–4840, 2018, doi: 10.1021/jacs.7b12818.

[58] C. Guo *et al.*, "Molecular Orbital Gating Surface-Enhanced Raman Scattering," *ACS Nano*, vol. 12, no. 11, pp. 11229–11235, 2018, doi: 10.1021/acsnano.8b05826.

[59] D. R. Ward, D. A. Corley, J. M. Tour, and D. Natelson, “Vibrational and electronic heating in nanoscale junctions,” *Nat. Nanotechnol.*, vol. 6, no. 1, pp. 33–38, 2011, doi: 10.1038/nnano.2010.240.

[60] B. Ren, G. Picardi, and B. Pettinger, “Preparation of gold tips suitable for tip-enhanced Raman spectroscopy and light emission by electrochemical etching,” *Rev. Sci. Instrum.*, vol. 75, no. 4, pp. 837–841, 2004, doi: 10.1063/1.1688442.

[61] R. Ramachandran, H. B. Li, W. Y. Lo, A. Neshchadin, L. Yu, and J. Hihath, “An Electromechanical Approach to Understanding Binding Configurations in Single-Molecule Devices,” *Nano Lett.*, vol. 18, no. 10, pp. 6638–6644, 2018, doi: 10.1021/acs.nanolett.8b03415.

[62] M. J. Frisch *et al.*, “Gaussian 09, Revision B.01,” *Gaussian 09 Revis. B01 Gaussian Inc Wallingford CT*, 2009.

[63] J. Qi, N. Edirisinghe, M. G. Rabbani, and M. P. Anantram, “Unified model for conductance through DNA with the Landauer-Büttiker formalism,” *Phys. Rev. B - Condens. Matter Mater. Phys.*, vol. 87, no. 8, pp. 1–10, 2013, doi: 10.1103/PhysRevB.87.085404.

[64] H. Rascón-Ramos, J. M. Artés, Y. Li, and J. Hihath, “Binding configurations and intramolecular strain in single-molecule devices,” *Nat. Mater.*, vol. 14, no. 5, pp. 517–522, May 2015, doi: 10.1038/nmat4216.

[65] Z. Li, L. Mejía, J. Marrs, H. Jeong, J. Hihath, and I. Franco, “Understanding the Conductance Dispersion of Single-Molecule Junctions,” *J. Phys. Chem. C*, vol. 125, no. 6, pp. 3406–3414, Feb. 2021, doi: 10.1021/acs.jpcc.0c08428.

[66] A. Troisi and M. A. Ratner, “Propensity rules for inelastic electron tunneling spectroscopy of single-molecule transport junctions,” *J. Chem. Phys.*, vol. 125, no. 21, 2006, doi: 10.1063/1.2390698.

[67] M. Paulsson, T. Frederiksen, H. Ueba, N. Lorente, and M. Brandbyge, “Unified description of inelastic propensity rules for electron transport through nanoscale junctions,” *Phys. Rev. Lett.*, vol. 100, no. 22, 2008, doi: 10.1103/PhysRevLett.100.226604.

[68] J. Im, S. Sen, S. Lindsay, and P. Zhang, “Recognition Tunneling of Canonical and Modified RNA Nucleotides for Their Identification with the Aid of Machine Learning,” *ACS Nano*, vol. 12, no. 7, pp. 7067–7075, Jul. 2018, doi: 10.1021/acsnano.8b02819.

[69] T. Hansen, G. C. Solomon, D. Q. Andrews, and M. A. Ratner, “Interfering pathways in benzene: An analytical treatment,” *J. Chem. Phys.*, vol. 131, no. 19, 2009, doi: 10.1063/1.3259548.

List of Publications:

[1] Taher Ghomian, Orthan Kizilkaya, Lucas Domulevicz, and Joshua Hihath, “Molecular quantum interference effects on thermopower in hybrid 2-dimensional monolayers”, ***Nanoscale*** 2022.

[2] Lucas Domulevicz, Hyunhak Jeong, Nayan Kumar Paul, Juan Sebastian Gomez-Diaz, and Joshua Hihath, “Multidimensional Characterization of Single-Molecule Dynamics in a Plasmonic Nanocavity”, **Angewandte Chemie** 2021.

[3] Book Chapter: Nadim Darwish, Cina Foroutan-Nejad, Lucas Domulevicz, Joshua Hihath, and Ismael Díez-Pérez, “Chap. 9: Principles of Molecular Devices Operated by Electric Fields,” *Effects of Electric Fields on Structure and Reactivity*, **Roy. Soc. of Chem.** March, 2021

[4] Haipeng B. Li, Yan-Feng Xi, Ze-Wen Hong, Jingxian Yu, Xiao-Xia Li, Wen-Xia Liu, Lucas Domulevicz, Shan Jin, Xiao-Shun Zhou, and Joshua Hihath, “Temperature-Dependent Tunneling in Furan Oligomer Single-Molecule Junctions”, **ACS Sensors** 2021.

[5] Hyunhak Jeong, Lucas Domulevicz, and Joshua Hihath, "Design and Fabrication of a MEMS-Based Break Junction Device for Mechanical Strain-Correlated Optical Characterization of a Single-Molecule", **IEEE J. Microelectromech. Syst.** (2020).

[6] Hyunhak Jeong, Haipeng B. Li, Lucas Domulevicz, and Joshua Hihath, “An On-Chip Break Junction System for Combined Single-Molecule Conductance and Raman Spectroscopies”, **Adv. Funct. Mater.** 2020, 30, 2000615

[7] Cliff E. McCold, Lucas Domulevicz, Zhengxu Cai, Wai-Yip Lo, Sahar Hihath, Katia March, Hashem M. Mohammad, M. P. Anantram, Luping Yu, and Joshua Hihath, “Molecular Control of Charge Carrier and Seebeck Coefficient in Hybrid Two-Dimensional Nanoparticle Superlattices”, **J. Phys. Chem. C** 2020, 174, 1, 17 - 24